International Journal of Plasticity 157 (2022) 103389

Contents lists available at ScienceDirect

International Journal of Plasticity

journal homepage: www.elsevier.com/locate/ijplas

Phase transition in medium entropy alloy CoCrNi under quasi-isentropic compression

Zhuocheng Xie [a,b], Wu-Rong Jian [c,*], Shuozhi Xu [d], Irene J. Beyerlein [d,e], Xiaoqing Zhang [a,b], Xiaohu Yao [a,b,*], Run Zhang [a,b]

[a] State Key Laboratory of Subtropical Building Science, South China University of Technology, Guangzhou, Guangdong 510640, PR China
[b] Department of Engineering Mechanics, South China University of Technology, Guangzhou, Guangdong 510640, PR China
[c] Department of Mechanical Engineering, Stanford University, Stanford, CA 94305, USA
[d] Department of Mechanical Engineering, University of California, Santa Barbara, CA 93106-5070, USA
[e] Materials Department, University of California, Santa Barbara, CA 93106-5050, USA

ARTICLE INFO

Keywords:
Plastic deformation
Phase transition
Chemical short-range order
Quasi-isentropic compression
Medium entropy alloy

ABSTRACT

Under high strain-rate loading, prominent increases in pressure usually triggers phase transition (PT), but the concomitant temperature rise may also cause melting. Quasi-isentropic (QI) compression provides a strategy to explore solid-state phase transition by reducing the temperature rise while retaining high pressure. Using large-scale molecular dynamics simulations, we investigate PTs in single crystal CoCrNi medium entropy alloys (MEAs) under QI compression. With the applied strain rates ranging from 10^8 s^{-1} to 10^{11} s^{-1}, the strain-rate dependence and anisotropy of yield stress and solid-state PT path are revealed by comparing the mechanical responses along three compressed crystallographic orientations ([100], [1$\bar{1}$0], and [111]). Positive strain-rate sensitiveness is found in the yield stress along the [1$\bar{1}$0] and [111] directions, while insensitiveness along the [100] direction. Various PTs occur alongside massive plastic deformation in the post-yield regime. As the strain rate rises, face-centered-cubic (FCC) to body-centered-cubic (BCC) PT overrides the stacking fault-induced hexagonal-close-packed (HCP) phase formation and dominates the plasticity for the [100] loading. By contrast, crystalline PTs give way to amorphization for [1$\bar{1}$0] and [111] loading at high strain rates. Chemical short-range order hinders dislocation slip and promotes dislocation interactions, which further facilitate early formation of the BCC phase, suggesting a potential strategy to tailor polymorphism in MEAs.

1. Introduction

With the development of transportation and defense technologies, there exists an increasing demand for robust structural materials in extreme environments. Providing a possible solution are multi-principal element alloys (MPEAs), which include both high entropy alloys (HEAs) and medium entropy alloys (MEAs) (Li et al., 2021b). They have attracted much attention due to their outstanding mechanical properties in many kinds of extreme conditions, such as excellent corrosion and irradiation resistance (Qiu et al., 2019; Shi et al., 2017; Kumar et al., 2016; El-Atwani et al., 2019), high Hugoniot elastic limits (Zhang et al., 2022), high phase transition (PT) threshold stresses (Jiang et al., 2016), and high spall strengths under shock loadings (Yang et al., 2020c,b). Recently, the series of CoCrNi-based MPEAs have demonstrated not only impressive fracture toughness and tensile strength at cryogenic

* Corresponding authors.
E-mail addresses: wurong@stanford.edu (W.-R. Jian), yaoxh@scut.edu.cn (X. Yao).

https://doi.org/10.1016/j.ijplas.2022.103389
Received 29 April 2022; Received in revised form 1 July 2022
Available online 20 July 2022

temperatures (Uzer et al., 2018; Gludovatz et al., 2016, 2014; Wu et al., 2018; Li et al., 2022; Liu et al., 2021), but also high tensile and shear strengths under dynamic loading (Ma et al., 2018; Zhang et al., 2020a; Li et al., 2018b, 2017b).

The vast design freedom on the composition of MPEAs produces various local chemical fluctuations, which can lead to intense dislocation activities and different PT processes (Maity et al., 2018; Ming et al., 2019; Schneider et al., 2020; Zhang et al., 2021; Bahramyan et al., 2020; Hasan et al., 2019; Chandan et al., 2022; Li et al., 2020; He et al., 2021b), including the FCC to hexagonal-close-packed (HCP) PT (Miao et al., 2017), FCC to HCP to body-centered-cubic (BCC) PT (Bae et al., 2018), and amorphization (Zhao et al., 2021b). For example, it was found that increasing the content of Co decreases the stacking fault (SF) energy of the FeCoNiCrMn HEA. This change promoted a PT from the parent FCC phase to a newly formed HCP phase (Liu et al., 2019). Similarly, introducing a small amount of Si, C, and Al elements was found to lower the stability of the FCC phase, triggering the FCC-HCP PT in CoCrNi-based MPEAs (Nene et al., 2018a,b; Chen et al., 2018). The authors reported that the HCP phase not only acts as a reinforcement via providing phase boundaries to prevent dislocation glide, but also contributes to the total elongation via sharing the load from the plastically deforming FCC phase. In a related sense, based on tensile experiments, HCP phase nucleates and grows at the SF networks in the FCC phase, serving as the major source of strain hardening (Miao et al., 2017; Slone et al., 2018; Chen et al., 2020; He et al., 2021a; Kim et al., 2022). This type of PT also aids in dynamic grain refinement and significantly enhances strength under dynamic shear loading (Ma et al., 2018). On the computational side, a series of molecular dynamics (MD) simulations were performed to further elucidate the underlying mechanisms of FCC-HCP PT in CoCrNi-based MPEAs (Fang et al., 2019; Hsieh et al., 2020; Qi et al., 2021; Xiao and Deng, 2020). Fang et al. (2019) studied the reversibility of the FCC-HCP PT and its relation to slip-induced SF formation and annihilation in both the FCC and HCP phases, which improves the plasticity of HCP grains and contributes to work hardening during tensile loading. In simulating the FCC-HCP PT in single crystal CrMnFeCoNi HEA nanowires, Xiao and Deng (2020) reported a PT-induced superplasticity and strengthening that results from continuous dislocation nucleation and propagation from the nanowire free surfaces.

Another type of PT, the FCC-HCP-BCC PT, has also been investigated in FCC CoCrNi-based MPEAs. An experimental study of VCrFeCoNi HEA by Jo et al. (2019) found that the HCP phase forms early in the deformation and then acts as a nucleation site for the subsequent BCC phase. A similar result was reported by Bae et al. (2018) in $Fe_{60}Co_{15}Ni_{15}Cr_{10}$ HEA. They noticed that shear bands are generated inside the grains after yielding, followed by the formation of BCC phase where two non-planar shear bands intersect. In addition, they reported that the BCC phase can also nucleate at grain boundaries (GBs) after yielding, which they attributed to the high excess energy of GBs. Like the HCP phase in FCC-HCP PT, BCC phase formation and the concurrent load partitioning between the FCC and BCC phases contribute to the increase in strength and promote strain hardening. Yang et al. (2020a) tailored the Mn content of $Fe_{45}Co_{30}Cr_{10}V_{10}Ni_{5-x}Mn_x$ (x = 0, 2.5, and 5) and reported that the increased Mn content reduces the critical strain required to trigger the FCC-HCP-BCC PT and consequently enhances the transformation rate. The large proportion of the BCC phase which possess many available slip systems leads to sustainable high strain hardening rate and consequently delays the tensile instability. As a result, this transformation-induced plasticity (TRIP)-assisted MPEAs possess an excellent combination of high strength and good ductility (Li et al., 2016, 2017a; Zhang et al., 2020c).

Solid-state amorphization also occurs in deformed CoCrNi-based MPEAs. Ming et al. (2020) found that amorphous bands are activated in FCC-structured $Cr_{26}Mn_{20}$-$Fe_{20}Co_{20}Ni_{14}$ MPEA during low-temperature tensile deformation. Besides, these nanoscale bands possess high thermal stability, making possible its co-deformation with the FCC matrix and thus leading to the increase in strain hardening capacity without sacrificing yield strength at elevated temperatures. Recently, Zhao et al. (2021b) reported that amorphous islands can be generated in CrMnFeCoNi HEA at regions where a critical dislocation density is reached under severe compression and shear tests. By promoting additional strengthening and/or toughening, these amorphous regions enhance the resistance of material to high strain-rate loading. Wang et al. (2021) further proposed that such solid-state amorphization stems from both high lattice friction and high GB resistance to dislocation glide. They also observed the formation of amorphous nanobridges in the crack wake, which provided a rationalization for the effective toughening by the amorphization processes.

In summary, the ability for MPEAs to transform into various crystalline structures and an amorphous state (Moulton and Zaworotko, 2001; Sheng et al., 2007; Zeng et al., 2010) not only indicates the nature of metastability of these alloys, but also provides an open avenue to explore the potential and suitability for this material for high strain-rate loading and large deformation.

Although numerous studies have focused on PT in MPEAs, they mainly reported one or two PT processes in these alloys, or used PT as a way to produce new compositions. A detailed exploration of different PT processes in a certain MPEA is still missing. For extreme loading conditions, increases in pressure and temperature are usually coupled, while structural transitions is more sensitive to pressure when the temperature is below melting point (Jian et al., 2022). Recent experimental investigations of PT in MPEAs found that pressure plays a more significant role in activating PT, compared to temperature (Zhang et al., 2017; Tracy et al., 2017), which further raises the necessity to uncouple these two factors in terms of clarifying PT mechanisms in extreme regimes. In addition, it should also be noted that the corresponding mechanical responses and deformation behavior in extreme regimes are normally strain-rate dependent.

Experimentally, static high-pressure loading using a diamond anvil cell (DAC) and shock loading by gas-gun driven or laser driven systems are two common and effective ways to explore the extreme states of materials, apart from the fact that they represent two different thermodynamic loading paths. On the one hand, static high-pressure loading via a DAC at a constant temperature is an isothermal process due to the sufficient heat transfer with the surroundings, as shown by blue curves in Fig. 1(a). On the other hand, shock loading is generally regarded as an adiabatic process since the transient loading provides a short duration for the system to transfer heat with the ambient air, which results in a coupled state of large stress and high temperature in the material, as denoted by the gray dashed line in Fig. 1(a). If an adiabatic process were reversible, the process would be referred to as an isentropic process, as shown by the vertical gray dashed line in Fig. 1(b). However, a loading path always tends to increase the entropy of the system

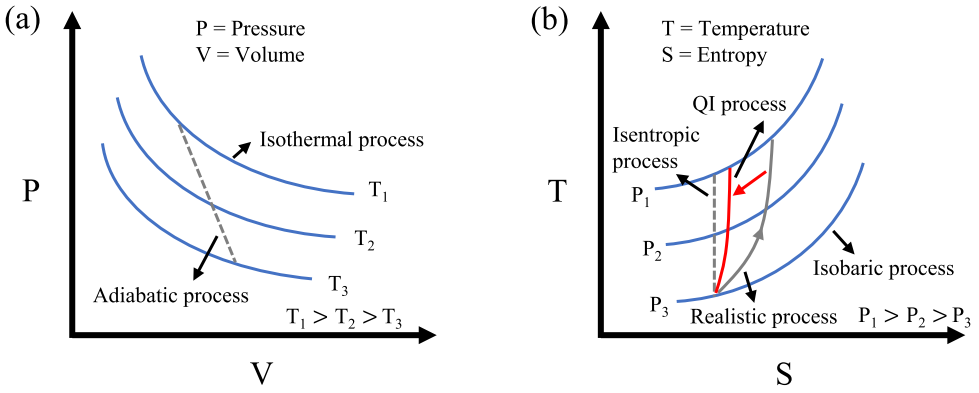

Fig. 1. (a) Pressure (P)-volume (V) and (b) temperature (T)-entropy (S) diagrams to illustrate the processes of different thermodynamic loading paths. The red arrow in (b) denotes a realistic process approximating the isentropic process, which is described as the quasi-isentropic (QI) process (red solid line). (For interpretation of the references to color in this figure legend, the reader is referred to the web version of this article.)

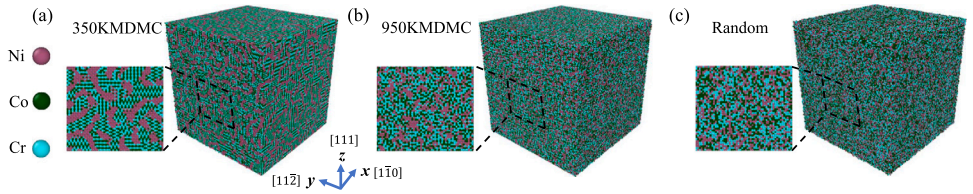

Fig. 2. Atomic configurations for 350KMDMC, 950KMDMC, and random CoCrNi samples. Here, 350KMDMC and 950KMDMC denote the samples annealed at 350 K and 950 K during the hybrid MD/MC simulations, respectively. Random refers to the sample with an ideally uniform random atomic distribution.

(i.e., the second law of thermodynamics), as displayed by the gray solid curve in Fig. 1(b). Supposing that a thermodynamic loading path maintains an increase in pressure from P_3 to P_1, but with less temperature rise, the gray solid line will approximate the gray dashed line as shown by the red arrow in Fig. 1(b). Therefore, the corresponding process can be described as quasi-isentropic (QI) compression (red solid line), which means that the loading increases the temperature of the system but at a much lower rate than shock compression. The QI loading path provides a strategy to uncouple the effects of stress and temperature at high strain rates to some extent, and it has been widely used to investigate both experimentally and in simulation the dynamic behavior of materials under explosive wave deformation (Lorenz et al., 2006; Jarmakani et al., 2007; Vogler et al., 2009; Seagle et al., 2013; Luo et al., 2017; Higginbotham et al., 2012; Cai et al., 2015; Lane et al., 2016; Xiang et al., 2016; Wang et al., 2017).

Finally, we want to remark on the important role in deformation and defect evolution played by chemical short-range order (CSRO), a subject that has gained much attention by experimental and simulation studies (Ding et al., 2018; Antillon et al., 2020; Yin et al., 2020; Smith et al., 2020; Romero et al., 2022). Although the effect of CSRO on plastic deformation have been evidenced by experiments (Zhang et al., 2020b; Chen et al., 2021b; Zhou et al., 2022), and discussed by simulations under both constant strain-rate loading (Li et al., 2019; Jian et al., 2020) and shock loading (Xie et al., 2021), their role in PT has not been investigated to our best knowledge. Recent simulation work revealed that the local relative stability of FCC and BCC structures is sensitive to the local elemental concentration (Chen et al., 2021a). Their results further suggested that the FCC-BCC PT induced by CSRO leads to an enhancement of both the ultimate strength and ductility in the CoCuFeNiPd HEA. The above study proposes a promising strategy to design MPEAs with high-performance mechanical properties for engineering applications under extreme condition by tuning CSRO. Given that the PT is usually related to the external loading conditions (Bridgman, 1956), the relation between CSRO and the susceptibility of PT, and the effects of CSRO and strain rate on PT mechanisms in MPEAs, are important to understand.

In this work, using both hybrid Monte Carlo (MC)/MD and large-scale MD simulations, QI compression is performed to investigate the dynamic mechanical responses and underlying mechanisms of plastic deformation and polymorphic transition in single crystalline CoCrNi MEA at various strain rates. The CoCrNi MEA is chosen, since it is a representative MPEA with a combination of high strength and good ductility (Zhang et al., 2020b). The anisotropy and strain-rate dependence of plastic deformation, crystalline PTs and amorphization are revealed with respect to the effects of CSRO. Moreover, the microstructural evolution and the corresponding mechanisms are discussed to better understand the TRIP effect in MPEAs.

2. Methodology

The large-scale atomic/molecular massively parallel simulator (LAMMPS) is used for all MD simulations here (Plimpton, 1995). The atomic interactions within the MEA Co-Cr-Ni system are described by the embedded atom method (EAM) potential developed

Table 1
Schmid factors for the 12 slip systems for the [100], [1$\bar{1}$0], and [111] loading orientations.

Orientation	Slip system											
	$\frac{(111)}{[01\bar{1}]}$	$\frac{(111)}{[10\bar{1}]}$	$\frac{(111)}{[1\bar{1}0]}$	$\frac{(\bar{1}11)}{[01\bar{1}]}$	$\frac{(\bar{1}11)}{[101]}$	$\frac{(\bar{1}11)}{[110]}$	$\frac{(\bar{1}\bar{1}1)}{[011]}$	$\frac{(\bar{1}\bar{1}1)}{[101]}$	$\frac{(\bar{1}\bar{1}1)}{[1\bar{1}0]}$	$\frac{(1\bar{1}1)}{[011]}$	$\frac{(1\bar{1}1)}{[10\bar{1}]}$	$\frac{(1\bar{1}1)}{[110]}$
[100]	0	0.408	0.408	0	0.408	0.408	0	0.408	0.408	0	0.408	0.408
[1$\bar{1}$0]	0	0	0	0.408	0.408	0	0.408	0.408	0	0	0	0
[111]	0	0	0	0	0.272	0.272	0.272	0.272	0	0.272	0	0.272

Table 2
CSRO parameter α^1_{ij} of various MEA samples.

MEA	CSRO parameter					
	α^1_{NiNi}	α^1_{NiCo}	α^1_{NiCr}	α^1_{CoCo}	α^1_{CoCr}	α^1_{CrCr}
350KMDMC	0.4701	0.5566	0.3837	−0.0182	−0.5822	−0.1075
950KMDMC	0.1627	0.2184	0.1070	−0.0598	−0.3378	−0.1160
Random	−0.0011	0.0003	−0.0024	−0.0003	−0.0019	0.0010

by Li et al. (2019), which has been successfully used in a few recent MD studies involving defect evolution and plastic deformation (Li et al., 2019; Cao et al., 2020; Jian et al., 2020, 2022; Cao et al., 2021; Xie et al., 2021; Dai et al., 2021; Hua et al., 2021).

First, we build the atomic model of pure Ni that contains about 1.8 million atoms with dimensions of ~27 nm × 27 nm × 27 nm. Next, the Ni atoms are randomly substituted by Co or Cr atoms until the desired equal molar composition (Co:Cr:Ni = 1:1:1) is reached. This atomic model is referred to as the random CoCrNi MEA sample. To construct the atomic models of the MEAs with different degrees of CSRO, the pure Ni model is utilized in a hybrid MD and MC simulation under two different annealing temperatures (350 and 950 K). After the hybrid MD/MC simulation, 1/3 of all Ni atoms are replaced by Co or Cr atoms and we achieve an MEA configuration with the equimolar composition and CSRO. The details about the hybrid MD/MC simulation are the same as those in our prior studies (Jian et al., 2020; Xie et al., 2021; Jian et al., 2021). Here, we use "number+K+MDMC" to denote the sample obtained by hybrid MD/MC simulation at a specific annealing temperature.

To examine anisotropy in the deformation mechanisms, two sets of crystallographic orientation are chosen to construct the initial atomic configurations. The first set is oriented with its [100], [010], and [001] aligned respectively with the x-, y- and z-axes, while the combination of [1$\bar{1}$0], [11$\bar{2}$], and [111] respectively aligned along x-, y- and z-axes is utilized as the second set. Herein, [100], [1$\bar{1}$0] and [111] directions are the loading orientations. The three loading orientations are selected because the [100] direction is generally regarded as a soft direction, while the [111] direction is known as a geometrically hard direction and the [1$\bar{1}$0] direction is intermediate (Uzer et al., 2018; Laplanche et al., 2020; Li et al., 2022). Their respective Schmid factors for slips under uniaxial loading are provided in Table 1.

The CSRO is quantified by Warren–Cowley SRO parameters (Cowley, 1950; de Fontaine, 1971), $\alpha^n_{ij} = \frac{p^n_{ij} - c_j}{\delta_{ij} - c_j}$, where n means the nth nearest-neighbor shell of the central i-type atom, p^n_{ij} denotes the probability of a j-type atom being around an atom of type i within the nth shell, c_j is the concentration of j-type atom, and δ_{ij} is the Kronecker delta function. For α^n_{ij}, a value of zero represents a system with completely random atomic distribution. A positive α^n_{ij} for pairs of the same species (i.e., $i = j$) or a negative α^n_{ij} for those of different species (i.e., $i \neq j$) indicate a preference of local ordering between the corresponding atomic pairs. The larger positive values for same species pairs or larger negative values for unlike species pairs result in higher degrees of CSRO. Fig. 2 shows the atomic configurations for various CoCrNi MEAs with the first set of crystallographic orientations after the MD/MC procedure. As shown in Table 2, only $\alpha^1_{NiNi}/\alpha^1_{CoCr}$ exhibits large positive/negative value for same/unlike species pairs among all CSRO parameters of models after MD/MC procedure. We find that the random model in Fig. 2(c) has near-zero CSRO parameters, confirming expectation. The degree of CSRO increases with decreasing annealing temperature. Thus, the lower annealing temperature used in the 350KMDMC sample possesses the highest degree of CSRO (Fig. 2(a)), with the largest absolute values of both α^1_{CoCr} and α^1_{NiNi} among the three MEAs, corresponding to the local CoCr cluster and Ni segregation, respectively. All the CoCrNi MEAs have various CSRO degrees but almost the same lattice distortion, as reported in Jian et al. (2020).

Prior to loading, the energy of all atomistic structures is minimized and all samples are relaxed at 300 K for 100 ps under the NPT ensemble with three-dimensional periodic boundary conditions (PBCs) to reach an equilibrium state. Then, a wave-free QI compression is carried out to investigate the plastic deformation and PT mechanisms of MEAs. Such a loading technique was proposed by Ravelo et al. (2009) and has been used to study the dynamic responses of materials with consideration of strain rate effects (Levitas and Ravelo, 2012; Hahn et al., 2017; Li et al., 2021a). By applying homogeneous compression to the models at a constant strain rate, wave-free QI compression significantly reduces the computational cost with use of smaller simulation systems compared to those used in ramp wave compression. Yet it has proven to produce very similar structural states as those in the ramp wave compression for the same compressive strains at a similar strain rate (Hahn et al., 2017). Hence, through this method, we can feasibly expand the strain-rate range while maintaining acceptable computational costs. Here, we consider a strain-rate range from 10^8 s^{-1} to 10^{11} s^{-1} for uniaxial-strain loading along the [100], [1$\bar{1}$0], and [111] directions with the other two orthogonal strains keeping zero. During QI compression, a micro-canonical ensemble (NVE) and PBCs along all directions are adopted. The timestep for the above relaxation and loading simulations is set to 1 fs.

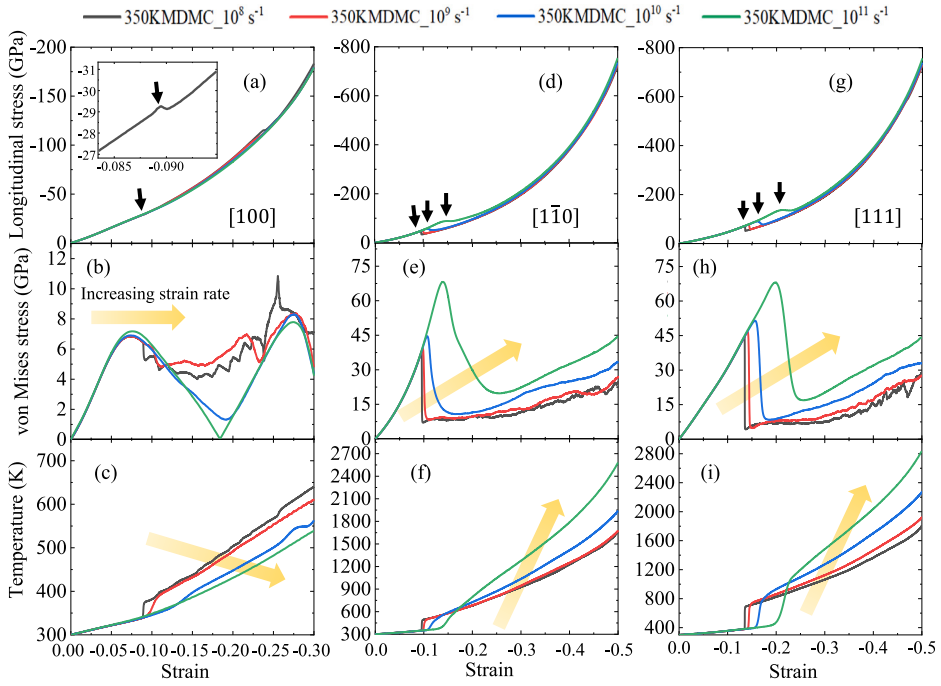

Fig. 3. (a), (d), (g) Longitudinal stress, (b), (e), (h) von Mises stress, and (c), (f), (i) temperature as functions of volumetric strain for the 350KMDMC MEA under QI compression at different strain rates from 10^8 s^{-1} to 10^{11} s^{-1} along [100], [1$\bar{1}$0] and[111] directions, respectively. The inflection points in longitudinal stress are denoted by black arrows in (a), (d), and (g).

To analyze the mechanical responses during the QI compression, the normal stress component along the loading direction of true Cauchy stress is adopted as the longitudinal stress, while the von Mises stress is used to characterize the plastic deformation. Besides, the average of normal stress components is calculated as pressure. To visualize our results and demonstrate the processes of defect evolution and PTs, the adaptive common neighbor analysis and dislocation analysis (DXA) method (Stukowski et al., 2012) implemented in OVITO (Stukowski, 2009) are applied.

3. Simulation results

3.1. Mechanical response during QI compression

Fig. 3 compares the longitudinal stress, von Mises stress, and the corresponding temperature rise as functions of volumetric strain for 350KMDMC MEA when tested in three crystallographic directions and at various strain rates. Similar responses for the other two MEAs are presented in Figure S1 and S2 of the supplementary material. As seen in Fig. 3(a,d,g), the effect of strain rate on compression along the [100] direction is not as pronounced as that along [1$\bar{1}$0] and [111] directions. In the latter cases, we observe an inflection point in longitudinal stress, denoted by the black arrow, which tends to be postponed at elevated strain rates. By contrast, the inflection point can only be seen in the curve for [100] loading at the strain rate of 10^8 s^{-1}. In Fig. 3(b,e,h), the von Mises stress declines sharply after its first rise, which indicates the onset of plastic deformation, and causes a rapid increase in temperature, as shown in Fig. 3(c,f,i).

With an increase in strain rate, the first peak value of von Mises stress, i.e., yield stress, and the corresponding critical strain display insensitivity to strain rate in the compression along [100] direction, as shown in Fig. 3(b). However, the post-yield stress development after the first drop varies with strain rate. For compression at the strain rates of 10^8 s^{-1} and 10^9 s^{-1}, serrated flow and strain hardening in the von Mises stress occur after yielding due to profuse plastic activities. In contrast, a relatively significant decline in von Mises stress is observed after yielding at the strain rate of 10^{10} s^{-1} with values as low as zero at the strain rate of 10^{11} s^{-1}, creating a hydrostatic compression state in the material. This implies a different plastic response after yielding compared to that at lower strain rates. Besides, strain hardening also arises during further compression. In Fig. 3(c), the temperature rise becomes moderate and smooth with increasing strain rates, indicating that the plastic deformation triggered at high strain rates is homogeneous, a point we will analyze next.

Compared with the [100] direction, different types of von Mises stress evolution are observed for the compression along [1$\bar{1}$0] and [111] directions. Denoted by the first von Mises peak stress, the yield stress shows positive strain-rate dependence in both [1$\bar{1}$0] and [111] (Fig. 3(e,h)). In particular, the yield stress decreases in the order of [111], [1$\bar{1}$0], and [100] when loaded at the same strain rate. The ranking is associated with both the value of Schmid factor and the number of available slip systems. As shown

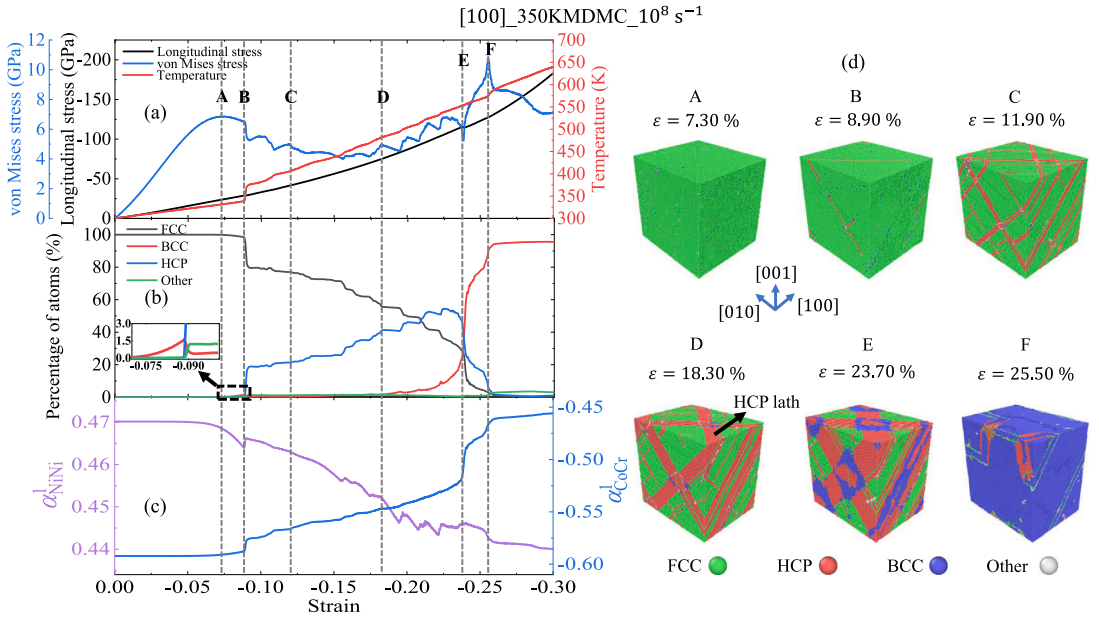

Fig. 4. The evolution of (a) von Mises stress, longitudinal stress, and temperature, (b) the percentages of different atomic types, and (c) the pairwise CSRO parameters α^1_{CoCr} and α^1_{NiNi} of the 350KMDMC MEA under QI compression along [100] direction at the strain rate of 10^8 s^{-1}. (d) displays six representative snapshots of the atomic configurations corresponding to the vertical dashed lines in (a)–(c). Here, face-centered cubic (FCC), body-centered cubic (BCC), hexagonal-close-packed (HCP) atoms, and those with unknown coordination structure are colored by green, blue, red, and white, respectively. (For interpretation of the references to color in this figure legend, the reader is referred to the web version of this article.)

in Table 1, with the smallest Schmid factor, the largest applied shear stress is required to activate dislocation slips along [111] among the three loading directions. On the contrary, it is easier to trigger dislocation slip in the other two directions due to larger Schmid factors. Moreover, the required applied stress is further reduced along the [100] direction compared to the $[1\bar{1}0]$ direction, since dislocations glide more easily with the four more available slip systems for the [100] loading than the $[1\bar{1}0]$ loading. In the post-yield stage, compression along the $[1\bar{1}0]$ and [111] directions shows a larger stress drop in von Mises stress and stronger strain hardening behavior with an increasing strain rate (Fig. 3(e,h)), leading to a more severe temperature rise (Fig. 3(f,i)) than that of the [100] loading at high strain rates. It should be mentioned that all MEAs maintain solid state during QI compression for all strain rates, (see Appendix A for the calculation of melting point). Hence, in what follows, we focus on the effects of stress (or pressure) and strain rate.

3.2. Deformation mechanisms of compression along [100] direction

3.2.1. The overall trend of plasticity

To clarify the relationship among mechanical response, defect formation, and CSRO evolution during QI compression, we select six representative snapshots of 350KMDMC MEA compressed along [100] direction at the strain rate of 10^8 s^{-1} as examples to illustrate the corresponding plastic deformation (Fig. 4).

Moment A is the precursor of plastic flow, at which scattered BCC clusters are observed before any dislocations or SFs form (Fig. 4(d)). A similar result has been reported in compression loading of CoCrNi MEA along [001] direction (Cao et al., 2020). That study revealed the formation of BCC clusters due to shortening of atomic bonding along [001] and thus the collapse of the initial FCC crystal structure. According to the Bain model (Bain and Dunkirk, 1924), compression of 20% along [001] and an expansion of 12% along ⟨110⟩ direction can convert an FCC lattice to a BCC lattice. This explains the preferred formation of BCC clusters in the initial deformation stage of QI compression along ⟨100⟩. We will exploit such structural transitions in the following section. After that, dislocation nucleates and glides on {111} planes, triggering a rapid drop of von Mises stress at moment B (Fig. 4(a)) and randomizing the atomic arrangement, which is manifested as the reduction in the absolute value of the pairwise CSRO parameters α^1_{CoCr} and α^1_{NiNi} (Fig. 4(c)). Moreover, the dislocation glide interrupts the growth of incipient BCC clusters as shown in the enlarged inset of Fig. 4(b), preventing these scattered BCC clusters from developing into BCC phase. Later, at moment C in Fig. 4(d) we find that dislocations prefer to glide on $(\bar{1}11)$ and $(11\bar{1})$ planes. In Moment D in Fig. 4(d) continuing slip on parallel glide planes causes the pileup of SFs, which produces HCP laths in the material (denoted by the black arrow). During this FCC-HCP PT (Moment C to D), the serrated flow of von Mises stress results from numerous interactions of dislocations and SFs, leading to further decreases of CSRO. Later, BCC phases initiate from the intersections of HCP laths and coalesce with the neighboring BCC embryos, resulting in the HCP-BCC PT (Moments E and F in Fig. 4(d)).

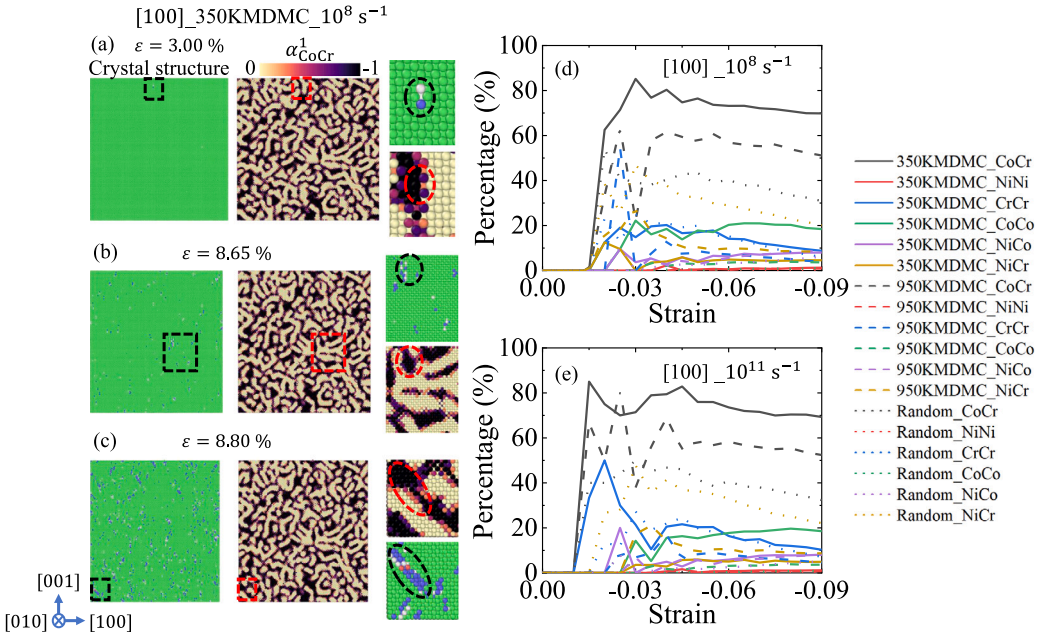

Fig. 5. Atomic distributions in the cross section of the 350KMDMC MEA under QI compression along the [100] direction at the volumetric strain of (a) 3.00%, (b) 8.65%, and (c) 8.80% at the strain rate of 10^8 s^{-1}. The atoms are colored according to their crystal structures (following Fig. 4) and the CSRO parameter α^1_{CoCr}. α^1_{CoCr} with more negative value means stronger CSRO. Regions marked by dashed rectangles are enlarged on the right side, where the correspondence between BCC clusters and CoCr-ordered regions is further denoted by dashed ellipses. (d)–(e) show the fraction of various atomic pairs within the BCC clusters of three MEAs during the initial compression stage at strain rates of 10^8 s^{-1} and 10^{11} s^{-1}, respectively. (For interpretation of the references to color in this figure legend, the reader is referred to the web version of this article.)

Comparing the FCC-HCP PT and the HCP-BCC PT, we see that the former PT activates plasticity and yields the material, while the latter is triggered by the accumulation of plastic deformation. The partitioning of stress among the newly-formed BCC phase and the pre-existing FCC and HCP phases results in prominent strain hardening behavior, characterized by the increase of the von Mises stress during HCP-BCC PT (Moment E to F in Fig. 4(a)). Once the plastic flow is activated in the BCC phase by subsequent loading, the von Mises stress decreases after moment F.

3.2.2. Effects of CSRO on the nucleation of incipient BCC clusters

We mentioned above that the scattered BCC clusters precede dislocation nucleation, which has been reported in both conventional alloys (Bryukhanov et al., 2015) and MPEAs (Cao et al., 2020; Chen et al., 2021a). To understand the effects of CSRO on the nucleation of BCC clusters and its relationship with incipient plasticity, snapshots of the nucleation of the BCC cluster and Shockley partial (SP) dislocation and their corresponding maps of α^1_{CoCr} distribution in the cross-section of 350KMDMC CoCrNi sample during the initial deformation stage (strain below 9%) for [100] loading are shown in Fig. 5(a)–(c). The selected regions are enlarged on the right side. As denoted by the dashed ellipses of these enlargements in Fig. 5(a,b), the BCC clusters prefer to nucleate in the CoCr-ordered regions. These clusters further serve as the precursors for SP dislocation nucleation, as shown by the enlargements in Fig. 5(c).

To further elucidate the dependence of BCC cluster nucleation on the local atomic environment, we analyze the fraction of various atomic pairs in the BCC clusters for all three types of MEAs and at differing strain rates from the beginning of QI compression to the stage of incipient dislocation nucleation. It should be mentioned that only atoms with an absolute CSRO value over 0.8 are counted as the corresponding atomic pairs, which means the same atom can be calculated more than once. For example, Fig. 5(d,e) present the statistical results at the strain rates of 10^8 s^{-1} and 10^{11} s^{-1}, respectively. It is seen that the fraction of CoCr cluster is the largest in the BCC clusters for each type of MEA during the initial deformation period, regardless of the strain rate. In addition, the formation of BCC cluster has a preference for the atomic environment of ordered CoCr regions. Based on our previous study, the CoCr region has a lower unstable stacking fault energy than the random CoCrNi MEA and pure Ni, which indicates that it is easier to form SFs in the CoCr aggregations (Jian et al., 2020). Thus, the nucleation of dislocation is aided by the formation of BCC clusters with large amounts of CoCr atomic pairs. With a higher degree of CSRO, the percentage of CoCr regions and thus BCC clusters increase, further promoting subsequent plastic deformation.

Since the nucleation of BCC clusters triggers the onset of plasticity where the yield stress is determined, and the nucleation event is similar at various strain rates, all three types of MEAs (with or without CSRO) exhibit strain-rate independence in yield stress, as shown in Fig. 3(b), Figure S1 (b) and Figure S2 (b).

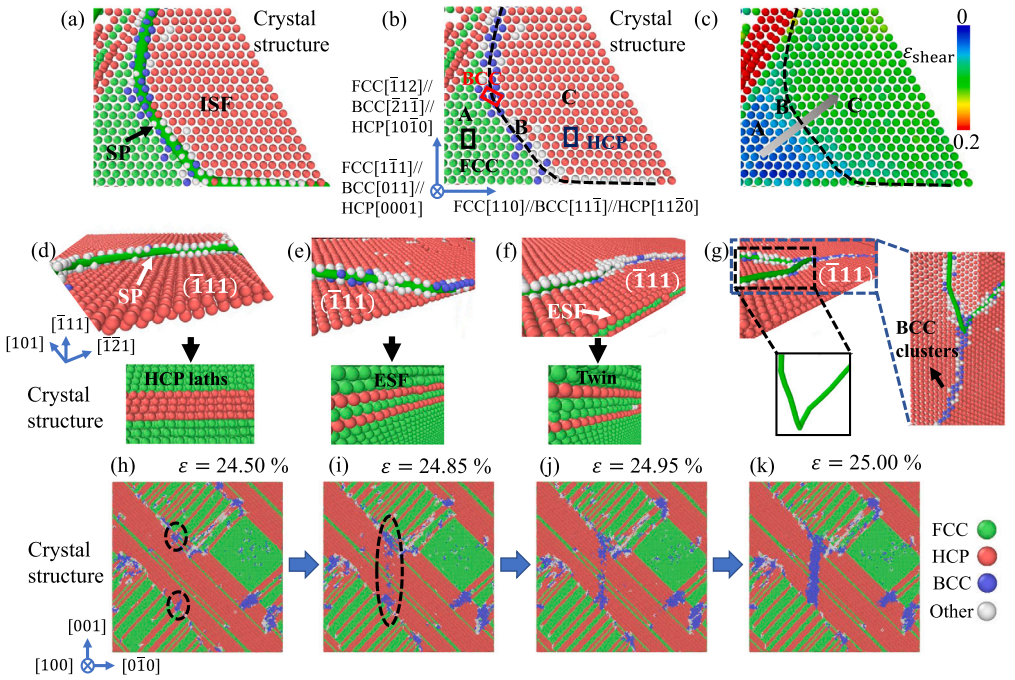

Fig. 6. Defect evolution in the 350KMDMC MEA under QI compression along the [100] direction at the strain rate of 10^8 s^{-1}: (a) Atomic configurations of SP dislocation propagation. (b) shows the corresponding indications of different lattice types near the SP dislocation and the orientation relationship, where region A is prior to SP, region B is the distorted area around SP dislocation, and region C is slipped by SP dislocation. (c) presents the atomic shear strain distribution. The SP dislocation is denoted by the green line in (a) and its position is indicated by the black dashed curve in (b) and (c). (d)–(g) show the formations of various microstructures via SP slip and interactions. (h)–(k) display the process of the formation of the BCC phase. (For interpretation of the references to color in this figure legend, the reader is referred to the web version of this article.)

3.2.3. Defect evolution and PTs

As straining continues and plastic deformation proceeds, many defects nucleate and interact. In Fig. 6(a), a SP dislocation that initiates from an incipient BCC cluster glides on the $(1\bar{1}1)$ plane in the FCC matrix, creates an intrinsic stacking fault (ISF), and generates distorted lattice structures around the SP dislocation. To better illustrate the relationship between the SP and these structures, the SP dislocation line in Fig. 6(a) is replaced by a black dashed curve in Fig. 6(b). It is seen that the region (region A) ahead of SP dislocation remains FCC structure, while around the SP dislocation, a mixture of BCC structure and non-crystalline lattice is observed (region B). The region behind the SP is an ISF that transitions to HCP stacking. It should be noted that the BCC lattices around SP dislocation are too small to be defined as BCC phases. Besides, the $(1\bar{1}1)$ plane and the [110] direction of the FCC lattice are respectively parallel to the (011) plane and the $[11\bar{1}]$ direction of the BCC lattice, and to the (0001) plane and the $[11\bar{2}0]$ direction of the HCP lattice, which corresponds to the Kurdyumov–Sachs (K–S) orientation relationship (Kurdjumov and Sachs, 1930; Yang et al., 2015). Previous research also reported a similar finding in FCC Cu and attributed such local FCC-BCC-HCP lattice rearrangement to the generation of excess atomic volume during the collective atomic displacement at the SP front (Korchuganov et al., 2019a,b). Similar to their results, the characteristic atomic displacement of region C induced by SP glide is the magnitude of a Burgers vector of $\frac{a}{6}[112]$, i.e., $b_p = \frac{\sqrt{6}}{6}a$, where a is the MEA lattice constant. However, the atomic displacement of region A is near zero. To coordinate the deformation between region A and C, the lattices in region B, which are contiguous to both FCC and HCP lattices, have the atomic displacement between zero to b_p. This is because they either deform into lattice cells with a similar aspect ratio as the BCC lattices or are distorted into non-crystalline lattices. After the SP propagates across the whole plane, all atoms will be displaced by b_p and the lattices of region A and B will transition into the HCP structure completely. As a result of such local lattice rearrangements via collective atomic displacement, the shear strain within region C with the formation of ISF after SP glide is larger than that around SP dislocation (region B), while there is almost no shear strain within the matrix (region A) within the FCC structure. This presents a strain gradient scenario across from regions A and B to region C (Fig. 6(c)).

After repeated SP dislocation slips and interactions, various microstructures form, as shown in Fig. 6(d–g). When SPs glide on every other {111} plane successively, HCP lathes form (Fig. 6(d)). When SPs glide on every {111} plane successively, an extrinsic stacking fault (ESF) or a twin forms (Fig. 6(e,f)). However, when two individual SPs gliding on the neighboring parallel {111} planes intersect, the overlapping parts of the two SPs annihilate and the BCC clusters that belonged to the original SP front are left behind (Fig. 6(g)). This phenomenon indicates that the intersection of SPs may seed BCC embryos, assisting BCC phase formation.

We further trace the formation of the BCC phase in Fig. 6(h–k). As mentioned above, the intersections of dislocations with HCP laths induce BCC nuclei, marked by the dashed ellipses in Fig. 6(h). The continuous nucleation and accumulation of dislocations

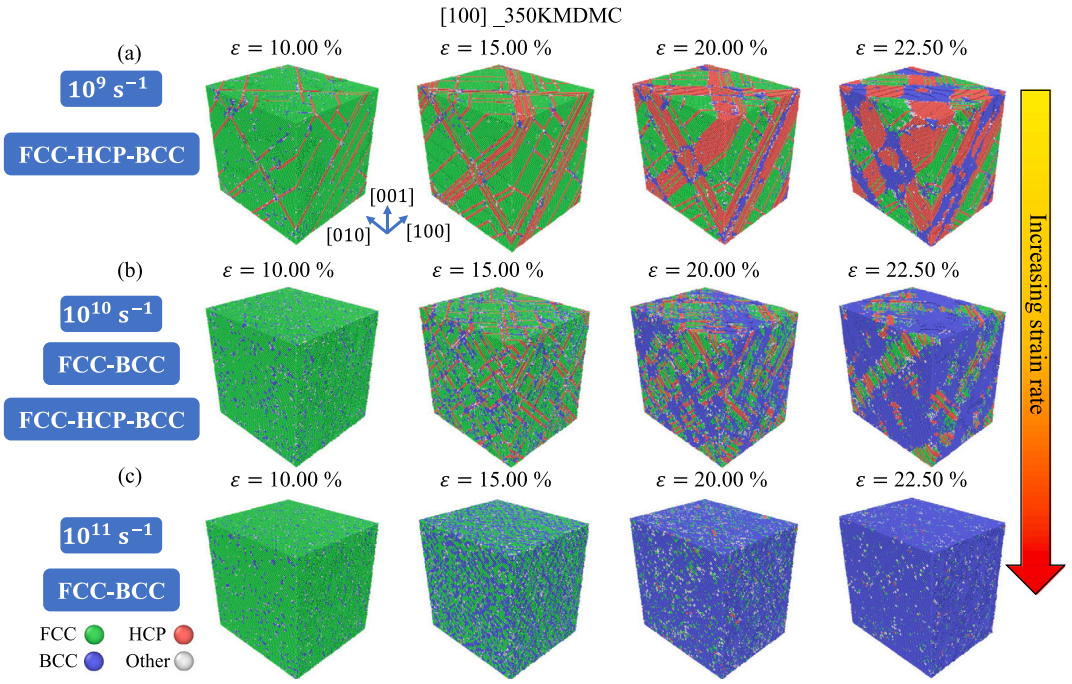

Fig. 7. (a)–(c) PTs in 350KMDMC MEA for the [100] loading at the strain rates from 10^9 s^{-1} to 10^{11} s^{-1}, where FCC-HCP-BCC PT is shown at the strain rates of 10^9 s^{-1} and 10^{10} s^{-1}, and FCC-BCC PT exists at the strain rates of 10^{10} s^{-1} and 10^{11} s^{-1}. The atomic coloring follows Fig. 4.

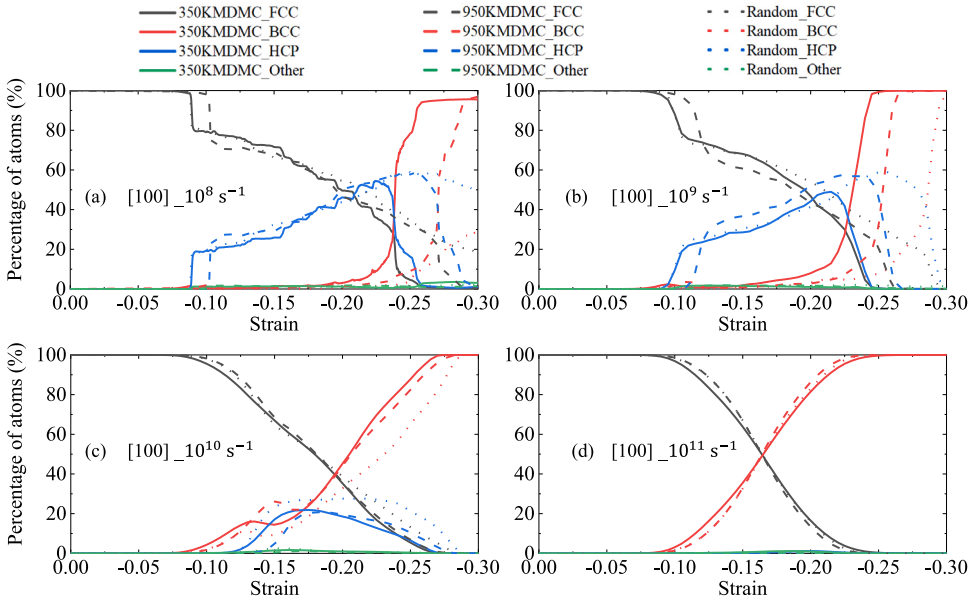

Fig. 8. The percentages of different atomic types as a function of strain under QI compression along [100] direction at different strain rates from 10^8 s^{-1} to 10^{11} s^{-1} in the three CoCrNi MEAs. Here, the definitions of atomic types and models follow Figs. 4 and 2, respectively.

around the HCP laths result in the propagation of the BCC regions. They further coalesce into a larger region of BCC phase, as denoted in the dashed ellipse in Fig. 6(i), leading to the FCC-HCP-BCC PT (Fig. 6(j,k)).

3.2.4. Strain-rate dependence of PTs with respect to CSRO effect

To clarify the effects of strain rate on PTs, Fig. 7 (a–c) compare the microstructural evolution of the 350KMDMC MEA at strain rates from 10^9 s^{-1} to 10^{11} s^{-1} during QI compression along [100]. Similar to the plastic responses at the strain rate of 10^8 s^{-1} shown

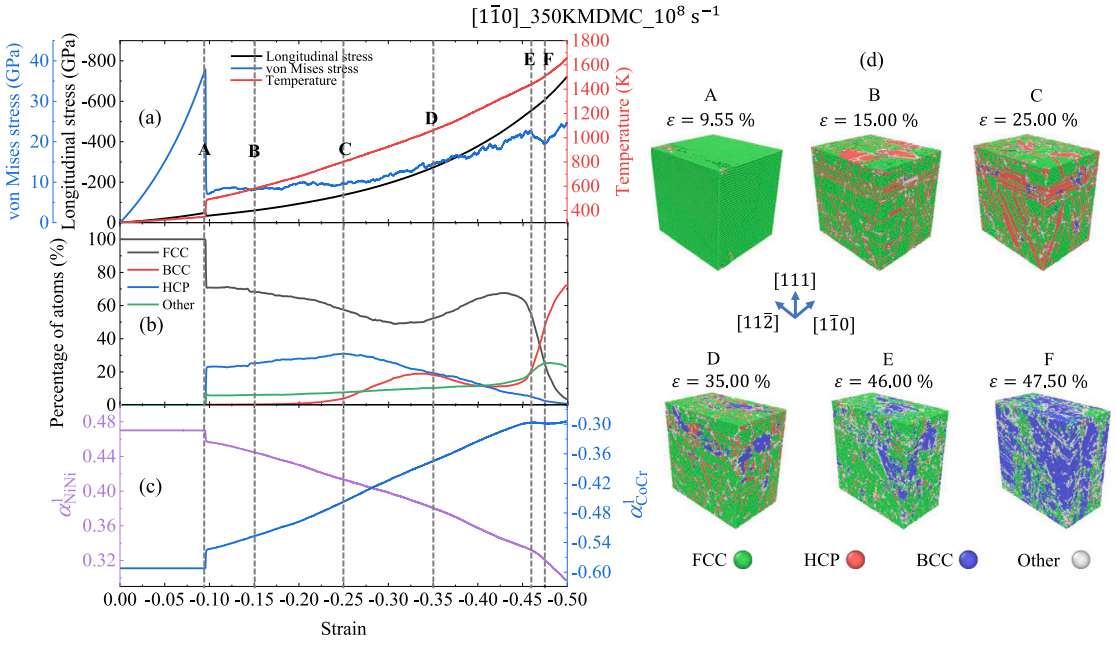

Fig. 9. The evolution of (a) von Mises stress, longitudinal stress and temperature, (b) the percentages of different atomic types, and (c) the pairwise CSRO parameters α^1_{CoCr} and α^1_{NiNi} of 350KMDMC MEA under QI compression along [1$\bar{1}$0] direction at the strain rate of 10^8 s^{-1}. (d) displays six representative snapshots of the atomic configurations corresponding to the vertical dashed lines in (a–c). Here, the atomic coloring follows Fig. 4 and the definition of 350KMDMC follows Fig. 2.

in Fig. 4(d), at the strain rate of 10^9 s^{-1}, numerous dislocations emerge from the scattered BCC clusters and glide on the {111} planes in the initial plastic stage during QI compression. Later, the SFs following behind SPs accumulate in the form of large HCP laths, and due to the interactions of these HCP laths, a BCC phase nucleates and then develops into a larger BCC crystal structure (Fig. 7(a)). As the strain rate increases to 10^{10} s^{-1}, BCC cluster development is promoted and with further straining FCC-BCC PT from the coalescence of incipient BCC clusters overrides the FCC-HCP-BCC PT (Fig. 7(b)). For this strain rate, it is worth mentioning that the development of the BCC region has two sources. On the one hand, the coalescence of a high-density BCC cluster stimulates the growth of the BCC phase in the initial stage. On the other hand, while some incipient BCC clusters transform into SFs early in the plastic deformation stage, the interaction of these SFs leads to the formation of more BCC nuclei via HCP-BCC PT in the later stages. These nuclei can coalesce with the existing BCC phases and accelerate the growth of the BCC regions (Fig. 8). At the strain rate of 10^{11} s^{-1}, dislocation activity is overwhelmed by homogeneous BCC nucleation (Figure S4) and the FCC-BCC PT dominates plastic deformation (Fig. 7(c)). Unlike the sharp temperature rise in the lower strain-rate regime induced by dislocation slip, which tends to suddenly release heat, the homogeneous structural transition process of FCC-BCC PT at high strain rate leads to a less intense temperature increase (Fig. 3(c)).

Since the incipient BCC clusters prefer to nucleate in the CoCr-ordered region in the initial deformation stage and the subsequent sluggish dislocation glide in ordered MEAs tends to generate BCC nuclei via dislocation interactions, it is more likely for the incipient BCC clusters and the BCC nuclei via dislocation interactions to further coalesce and form larger BCC regions in MEA with higher degree of CSRO as the compression proceeds. This speculation is confirmed in Fig. 8, where 350KMDMC model always has the earliest BCC phase formation than others at 10^8~10^9 s^{-1}, followed by 950KMDMC model and then random MEA. Nevertheless, these differences among these MEAs vanish with an increasing strain rate because higher strain rates promote homogeneous BCC nucleation in all MEAs (Fig. 8(c,d)).

3.3. Deformation mechanisms of compression along [1$\bar{1}$0] direction

3.3.1. The overall trend of plasticity

Similar to Section 3.2.1, the evolution of stress, temperature, the percentage of different atomic types and CSRO parameters of 350KMDMC MEA during QI compression along [1$\bar{1}$0] direction at the strain rate of 10^8 s^{-1} are studied in Fig. 9. In addition, six snapshots of atomic configurations are selected to demonstrate plastic deformation. The von Mises stress starts to drop at moment A due to the nucleation of dislocation. Prior to moment A, no incipient BCC clusters are activated in the FCC matrix, which is different from the case of [100] loading mentioned in Section 3.2.1, where the incipient BCC clusters appear before yielding. After that, as shown at moments B and C in Fig. 9(d), SPs glide with SFs following, which results in the decrease in the degree of CSRO (Fig. 9(c)) and in the amount of HCP ribbons. Next, in Moments C and D, BCC nuclei initiate HCP regions and these tiny BCC regions further grow and coalesce into a larger region of BCC phases (Moments E and F in Fig. 9(d)).

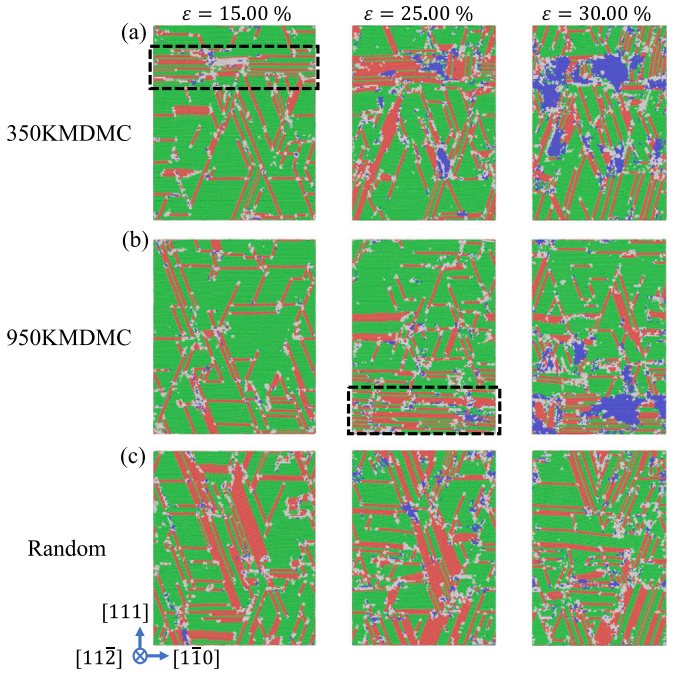

Fig. 10. Atomic distribution in the cross sections of (a) 350KMDMC MEA, (b) 950KMDMC MEA, and (c) random MEAs under QI compression along [1$\bar{1}$0] direction at the strain rate of 10^8 s^{-1}. The stacked fault structures is marked by black dashed rectangles. The atomic coloring follows Fig. 4.

Compared to the plastic responses of the [100] loading, the compression response of the [1$\bar{1}$0] loading (Figure S5(a)), profuse dislocation activities, instead of large HCP laths, are observed before the BCC phase grows. This results in more prominent twinning behavior via dislocation interactions for [1$\bar{1}$0] loading (Figure S6(a)) than [100] loading (Figure S4(a)). This preference for nanotwinning in CoCrNi MEA for [1$\bar{1}$0] loading has also been shown by both experiments and simulations (Uzer et al., 2018; Jian et al., 2020; Xie et al., 2021).

3.3.2. *Stacked fault structures related to CSRO*

Although dislocation multiplication and nanotwinning are prevalent in the initial plastic stage of compression along [1$\bar{1}$0], they are overridden by the formation of the BCC phase in the later stages of plastic deformation via frequent interactions of dislocations and SFs.

We compare the microstructural distribution of three types of MEAs and find that planar fault structures activate in all MEAs but their local features are different. For 350KMDMC MEA, planar slip on (1$\bar{1}$1) plane piles up to form HCP ribbons, as denoted by the dashed rectangle in Fig. 10(a). Later, more fault structures and dislocation storage occurs on parallel planes. We find that these stacked fault structures are comprised of multiple parallel SF arrays. These planar shaped structures later serve as strong obstacles to dislocations gliding on non-parallel planes. The interaction is seen to induce BCC nuclei, e.g., at $\epsilon = 25.00\%$. Finally, these BCC nuclei expand and coalesce into larger BCC phases at the strain of 30.00%. In contrast, in the 950KMDMC MEA, delayed stacked fault structures on (1$\bar{1}$1) plane and BCC nucleation occur, as denoted by the dashed rectangle in Fig. 10(b), while in the random MEA, a scattered distribution of fault structures appears and BCC phase nucleation becomes less active (Fig. 10(c)). The above difference is attributed to their differing degrees of CSRO. According to a previous study, a higher degree of CSRO results in stronger slip resistance to dislocation propagation and promotes dislocation planar slip (Zhang et al., 2020b), which increases the probability of dislocation interactions, further leading to earlier nucleation of BCC nuclei compared to MEAs with lower degrees of CSRO. Therefore, a higher CSRO degree is beneficial for BCC phase formation via FCC-HCP-BCC PT for [1$\bar{1}$0] loading. In this sense, the promotion of BCC phase nucleation by CSRO applies to both [100] and [1$\bar{1}$0] loadings.

3.3.3. *Strain-rate dependence of PTs with respect to CSRO effect*

We further explore the strain-rate dependence of PTs in [1$\bar{1}$0] loading. The microstructural evolution of 350KMDMC model during QI compression along [1$\bar{1}$0] direction at strain rates from 10^9 s^{-1} to 10^{11} s^{-1} is shown in Fig. 11(a–c). When compared with the FCC-HCP-BCC PT at the strain rate of 10^8 s^{-1} (Fig. 10(a)), we observe that abundant BCC nuclei form along with dislocations in the initial plastic deformation stage and develop into larger BCC phases in the later stage. It appears that deformation-induced FCC-HCP-BCC PT is facilitated by the higher strain rate of 10^9 s^{-1} (Fig. 11(a)). The coexistence of the FCC parent and HCP/BCC daughter phases leads to considerable stress partitioning. This is responsible for the strain hardening effect in the post-yield stage that follows the initial von Mises stress plateau in the strain range of 10% to 30% in Fig. 3(e). Besides the formation of the BCC phase

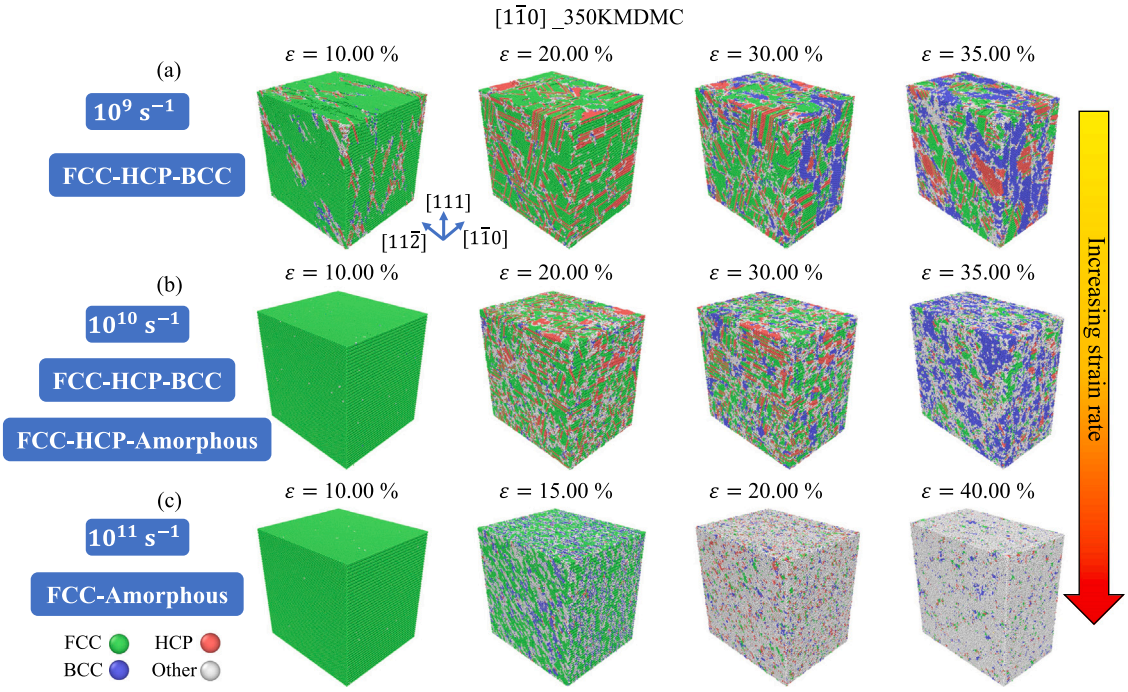

Fig. 11. (a–c) Evolution of PT in 350KMDMC MEA for [1$\bar{1}$0] loading at the strain rates from 10^9 s^{-1} to 10^{11} s^{-1}, where FCC-HCP-BCC PT is shown at the strain rates of 10^9 s^{-1} and 10^{10} s^{-1}, and FCC-HCP-amorphous appears at the strain rate of 10^{10} s^{-1}, while only FCC-amorphous PT exists at the strain rate of 10^{11} s^{-1}. The atomic coloring follows Fig. 4.

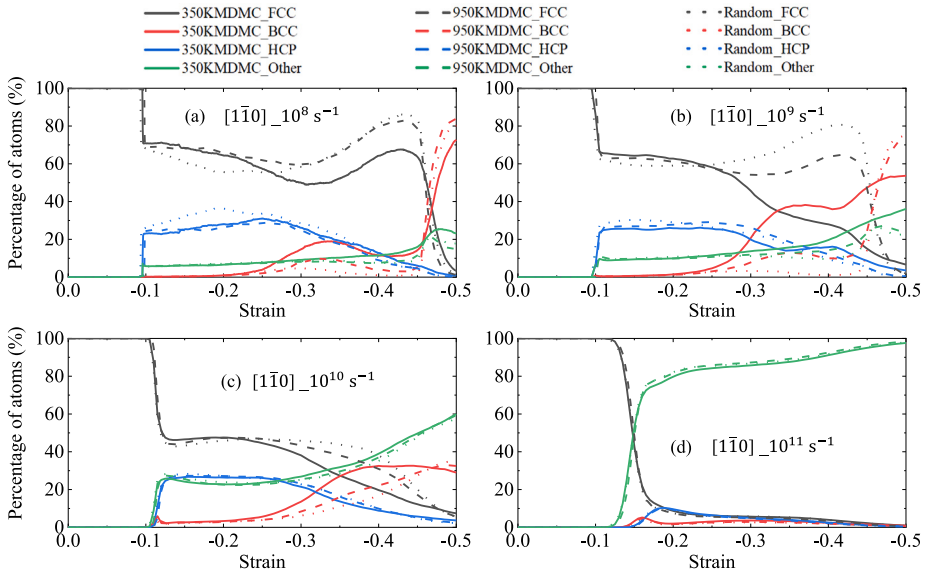

Fig. 12. The percentages of different atomic types as a function of strain under QI compression along [1$\bar{1}$0] direction at different strain rates from 10^8 s^{-1} to 10^{11} s^{-1} in the three CoCrNi MEAs. Here, the definitions of atomic types and models follow Figs. 4 and 2, respectively.

via FCC-HCP-BCC PT, more SP nucleate with the higher strain rate (Figure S5(c)) resulting in interactions between dislocation and SF (Fig. 11(b)). At the strain rate of 10^{10} s^{-1} (Fig. 12(c)), amorphous regions arise from the FCC-HCP-amorphous PT and their volume fractions rises significantly. Amorphization is due to the fact that the combination of the accumulation of defects and increasing deformation energy at higher strain rates aid in the nucleation of amorphous islands, as reported in both experimental and simulation work (Zhao et al., 2021b; Jian et al., 2022). At the strain rate of 10^{11} s^{-1}, amorphization becomes the dominant deformation mode

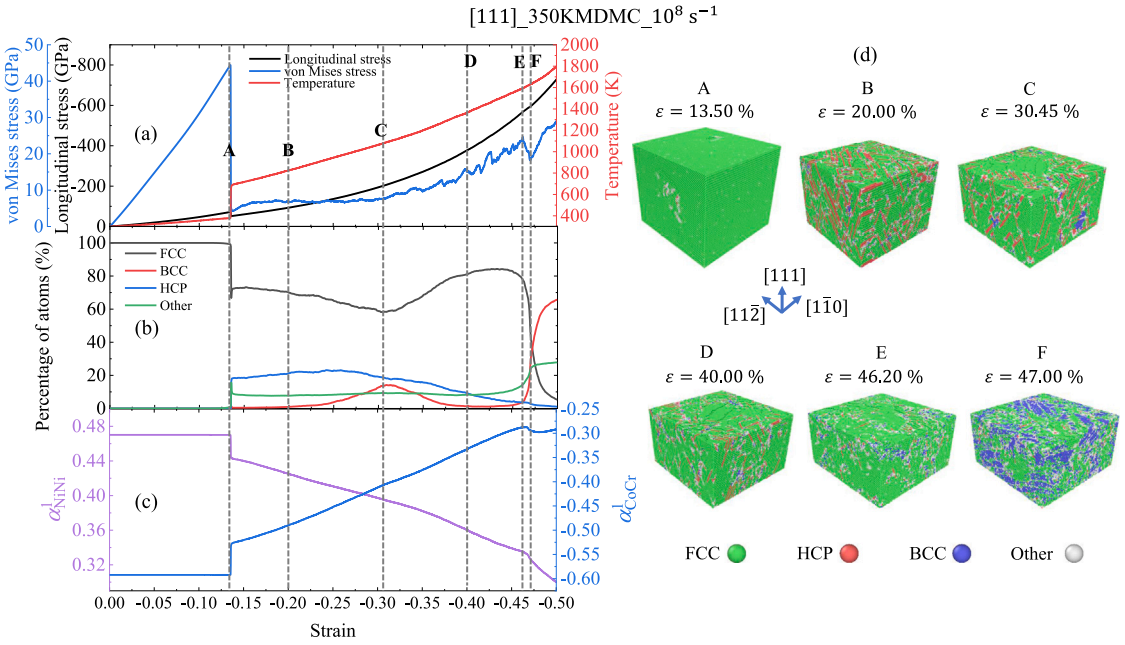

Fig. 13. The evolution of (a) von Mises stress, longitudinal stress and temperature, (b) the percentages of different atomic types, and (c) the pairwise CSRO parameters α^1_{CoCr} and α^1_{NiNi} of 350KMDMC MEA under QI compression along [111] direction at the strain rate of 10^8 s^{-1}. (d) displays six representative snapshots of the atomic configurations corresponding to the vertical dashed lines in (a–c). Here, the atomic coloring follows Fig. 4 and the definition of 350KMDMC follows Fig. 2.

to accommodate the large deformation that occurs in a very short time (Fig. 11(c)), which leads to an enhancement of yield stress and due to the release of massive deformation energy, a continually rising temperature (Fig. 3(e,f)).

The aforementioned viewpoint in Section 3.3.2 that CSRO promotes earlier FCC-HCP-BCC PT via frequent dislocation interactions also applies for [1$\bar{1}$0] loading at the strain rates from 10^8 s^{-1} to 10^{10} s^{-1} (Fig. 12(a–c)), in which the nucleation strain and rate for the BCC phase (from the FCC-HCP-BCC PT) decrease in the order of 350KMDMC, 950KMDMC, and random MEAs at the given strain rate. At a high strain rate of 10^{11} s^{-1}, however, MEAs with different CSRO degrees have quantitatively almost the same response in plastic deformation, i.e., the amorphization induced by high strain rate overwhelms dislocation activities and crystalline PTs, as shown in Fig. 12(d).

3.4. Deformation mechanisms in [111] compression

3.4.1. The overall trend of plasticity

Akin to Sections 3.2.1 and 3.3.1, the mechanical response and microstructure evolution of 350KMDMC MEA loaded along the [111] direction are also analyzed with respect to the evolution of stress, temperature, the percentage of different atomic types, and the CSRO parameters during QI compression. Further, to study structural evolution, in Fig. 13 we show six representative snapshots of atomic configurations. Similar mechanisms are seen between [111] loading and [1$\bar{1}$0] loading. In particular, dislocation nucleation triggers the onset of yielding at moment A and the sudden decrease of von Mises stress (Fig. 13(a)). Afterwards, a large number of SFs multiplies (Moment B in Fig. 13(d)), leading to the destruction of CSRO (Fig. 13(c)). The interactions of SFs give rise to BCC nuclei, denoted by the increase in the BCC atom percentage at Moment C (Fig. 13 (a,d)). However, SFs start to annihilate after moment C, which results in the disappearance of BCC clusters before they coalesce into larger BCC phase (Moment C,D in Fig. 13(b,d)). Such plastic response is rare in the [100] and [1$\bar{1}$0] loadings. The reasons will be discussed in the following analysis. With further compression, BCC phase initiates again at large strain and then grows in Moments E and F of Fig. 13(d), leading to the strain hardening behavior in Fig. 13(a).

It is worth mentioning that the CSRO variation is related to different PT paths under different loading orientations. As shown in Figs. 9(c) and 13(c), both [1$\bar{1}$0] and [111] loading shows similar decreasing trends of α_{CoCr} and α_{NiNi} in a smooth manner during the most of plastic deformation stage, since the FCC-HCP PT of this period proceeded by significant dislocation nucleation and slip events results in a prominent randomization of the atomic arrangement. In contrast, a serrated flow is observed in the CSRO-strain curve for [100] loading (Fig. 4(c)), especially when BCC phase begins to grow and expand, which competes with and finally overwhelms the dislocation activities of the prior FCC-HCP PT. Since FCC-HCP PT lasts for the most of plastic deformation stage for [1$\bar{1}$0] loading and [111] loading, while BCC phase nucleation is more significant for [100] loading, a more smooth and evident decrease of CSRO degree is observed in the former two loading orientations (Figs. 9(c) and 13(c)) than [100] direction (Fig. 4(c)).

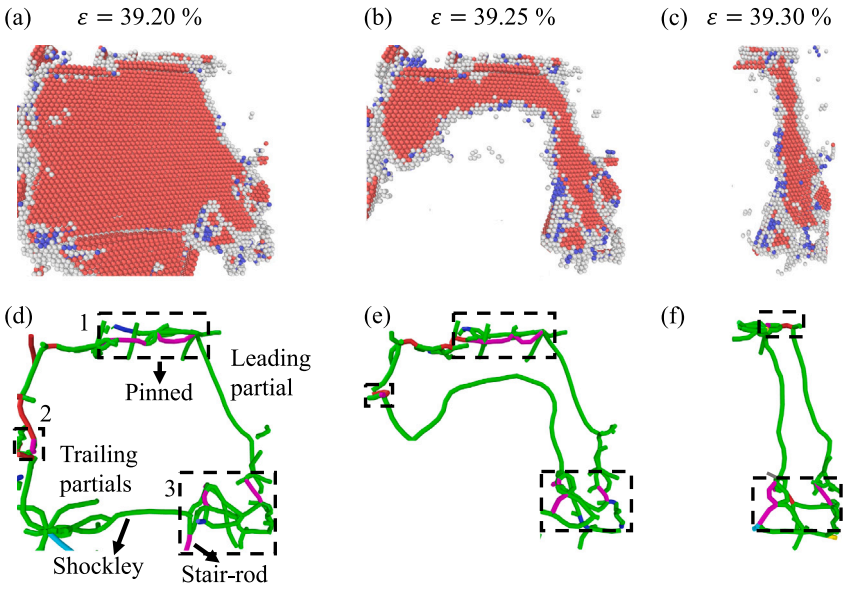

Fig. 14. Evolution of (a–c) SF regions and (d–f) dislocations during the process of SF annihilation in 350KMDMC MEA for [111] loading. The color scheme of crystal structure in (a–c) follows Fig. 4. In (d–f), the green lines denote SP dislocations, while the pink lines refer to stair-rod dislocations. These stair rods can pin the surrounding leading partial dislocations, as denoted by black dashed rectangles. (For interpretation of the references to color in this figure legend, the reader is referred to the web version of this article.)

3.4.2. SF annihilation

The SP densities of all MEAs exceed 7×10^{17} m^{-2} at the beginning of plastic deformation during [111] loading at the strain rate of 10^8 s^{-1}, compared to 3~4 $\times$ 10^{17} m^{-2} for [1$\bar{1}$0] loading and 0.5~1 $\times$ 10^{17} m^{-2} for [100] loading (Figures S3(a), S5(a), and S7(a)). On the one hand, profuse dislocation interactions nucleate BCC phases, as mentioned above. On the other hand, once the high dislocation density induces numerous dislocation junctions, the dislocation mobility decreases, which may lead to the annihilation of SFs. To demonstrate, a representative region in the 350KMDMC MEA is chosen to trace the evolution of SFs and dislocations. As shown in Fig. 14(a), frequent dislocation interactions produce sessile dislocation networks including stair-rods, marked by dashed rectangles in Fig. 14(d). These microstructures pin leading SPs and reducing the area of the bounded SF as the trailing SP glides forward (Fig. 14(b,c,e,f)). This pinning event is a frequent process during the compression in [111] in all three MEAs. It also reduces the probability of nanotwinning compared to the [1$\bar{1}$0] loading (Figure S8(a)). Thus, the content of HCP atoms decreases significantly before the BCC phase forms (Fig. 13(b)). However, as compression proceeds, the BCC phase nucleates again from the collective intersections of those pinned dislocations and takes the place of sluggish dislocation motion to carry subsequent plastic deformation (Moments D–F in Fig. 13(d)).

Compared to the FCC-HCP-BCC PT for [1$\bar{1}$0] loading, although the continuous growth of the BCC phase via FCC-HCP-BCC PT for [111] loading is interrupted by the disappearance of the BCC phase because of SF annihilation, subsequent BCC phase nucleation still resumes at those pinned dislocation intersections where profound plastic deformation accumulates. From this point of view, the mechanisms of BCC phase formation via FCC-HCP-BCC PT for both [1$\bar{1}$0] and [111] loadings are consistent, which also agree with the mechanisms of BCC phase nucleation from the HCP laths during FCC-HCP-BCC PT for the [100] loading in Section 3.2.3.

3.4.3. Strain-rate dependence of PTs with respect to CSRO effect

The strain-rate dependence of PTs for [111] loading is further explored in Fig. 15(a–c), which shows the microstructural evolution of 350KMDMC MEA at the strain rates from 10^9 s^{-1} to 10^{11} s^{-1}. Compared to the SP dislocation density at the initial plastic deformation stage (~7×10^{17} m^{-2}) at the strain rate of 10^8 s^{-1}, more SP dislocations nucleate at the onset of plastic stage (i.e., over 9×10^{17} m^{-2}) when loaded at the strain rate of 10^9 s^{-1} (Figure S7). As shown in Fig. 15(a), their frequent interactions first induce BCC clusters ($\epsilon = 30.00\%$) and later their entanglement leads to SF annihilation ($\epsilon = 42.50\%$). After this, amorphous clusters emerge, compensating for the declining dislocation activities, and BCC phase reappears, taking over plastic deformation up to a strain of 47.50%. With an increasing strain rate, more amorphous islands nucleate followed by significant interactions of dislocations and SFs (Fig. 15(b)). Amorphization dominates plastic deformation at the strain rate of 10^{11} s^{-1} (Fig. 15(c)), consistent with the strain-rate dependence of deformation and PTs for [1$\bar{1}$0] loading.

Similar to the promoting effects of CSRO on BCC phase nucleation mentioned in [100] and [1$\bar{1}$0] loading, since higher degrees of CSRO leads to slower dislocation glide, early nucleation of BCC clusters in 350KMDMC MEA is observed at the strain rates from 10^8 s^{-1} to 10^9 s^{-1} for [111] loading, while the BCC phase nucleation in 950KMDMC and random MEAs is comparatively retarded (Fig. 16). Nevertheless, these BCC nuclei vanish as SFs annihilate until they are reactivated to accommodate further deformation. Once the strain rate-induced amorphization initiates, all MEAs deform similarly at the strain rates of 10^{10} s^{-1} and 10^{11} s^{-1}, which present a remarkable strain hardening effect due to the additional strengthening effect of the amorphous phase (Fig. 3(h)).

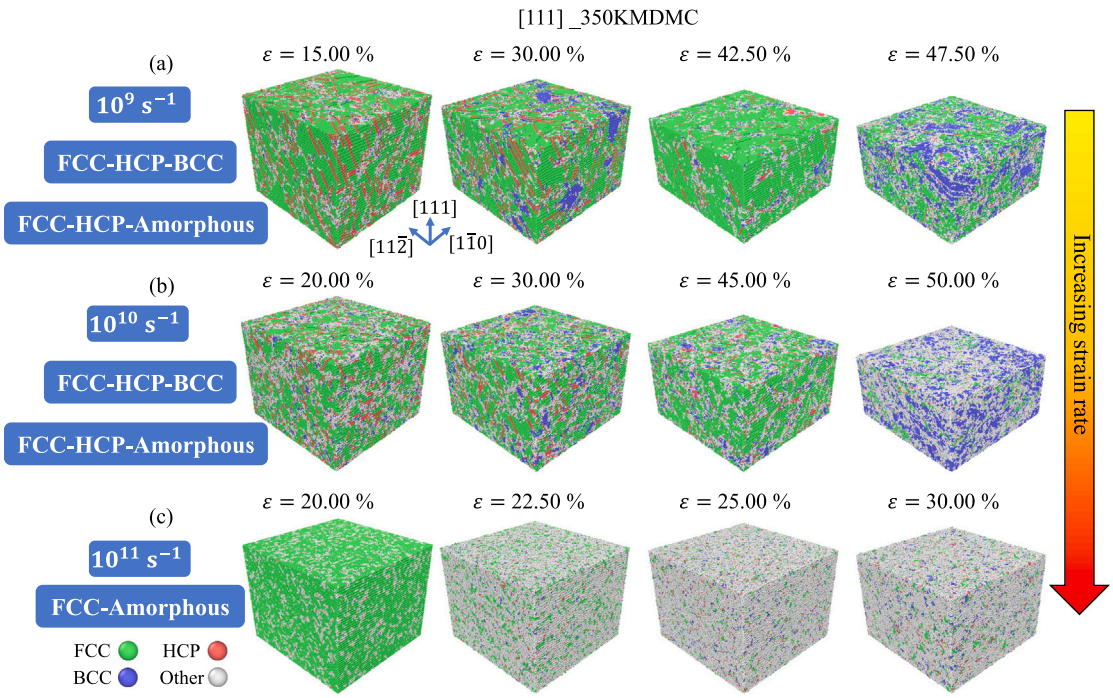

Fig. 15. (a)–(c) Evolution of PT in 350KMDMC MEA for [111] loading at the strain rates from 10^9 s^{-1} to 10^{11} s^{-1}, where FCC-HCP-BCC PT and FCC-HCP-amorphous PT both occur at the strain rates of 10^9 s^{-1} and 10^{10} s^{-1}, while only FCC-amorphous PT exists at the strain rate of 10^{11} s^{-1}. The atomic coloring follows Fig. 4.

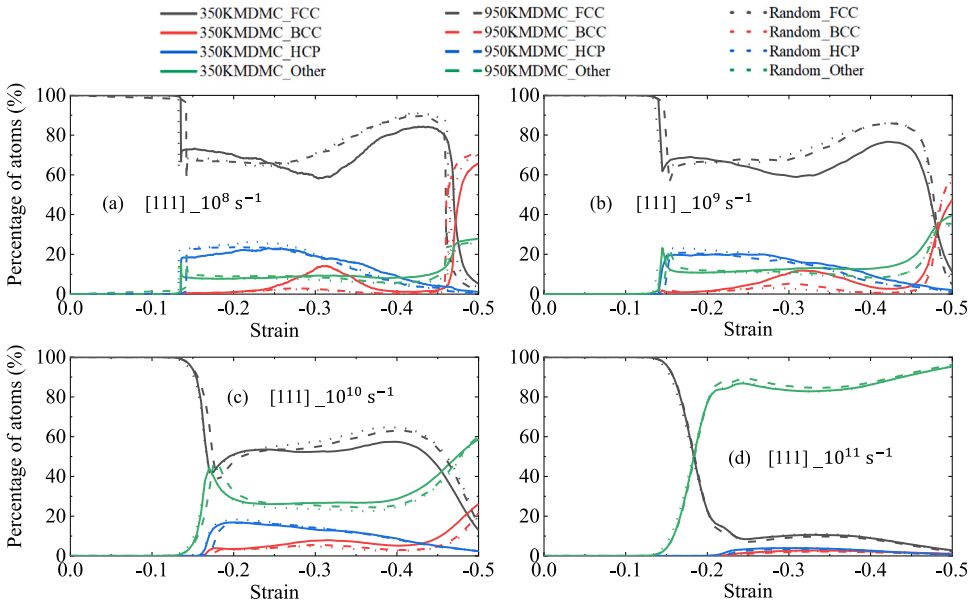

Fig. 16. The percentages of different atomic types as a function of strain under QI compression along [111] direction at different strain rates from 10^8 s^{-1} to 10^{11} s^{-1} in the three CoCrNi MEAs. Here, the definitions of atomic types and models follow Figs. 4 and 2, respectively.

3.5. *Summary of dependence of PT paths*

To summarize the dependence of PTs, we present the relationship between various PT paths and the conditions under which they occur (i.e., loading crystallographic orientation and applied strain rate) in Table 3. For all three loading orientations, only one PT path (FCC-HCP-BCC) happens at the strain rate of 10^8 s^{-1}. This PT path still dominates the deformation for the [100]

Table 3
Dependence of PTs on crystallographic orientation and strain rate in all MEAs.

Orientation	Strain rate (s^{-1})			
	10^8	10^9	10^{10}	10^{11}
[100]	FCC-HCP-BCC	FCC-HCP-BCC	FCC-BCC	FCC-BCC
$[1\bar{1}0]$	FCC-HCP-BCC	FCC-HCP-BCC	FCC-HCP-BCC FCC-HCP-Amorphous	FCC-Amorphous
[111]	FCC-HCP-BCC	FCC-HCP-BCC FCC-HCP-Amorphous	FCC-HCP-BCC FCC-HCP-Amorphous	FCC-Amorphous

and $[1\bar{1}0]$ loadings at the strain rate of 10^9 s^{-1}. However, another PT path (FCC-HCP-Amorphous) occurs to accommodate the plastic deformation for the [111] loading at the strain rate of $10^9 \sim 10^{10}$ s^{-1}, since dislocation mobility decreases due to severe dislocation entanglement. Unlike the [111] loading, in addition to FCC-HCP-BCC PT, FCC-BCC and FCC-HCP-Amorphous PTs emerge at the strain rate of 10^{10} s^{-1} for the [100] and $[1\bar{1}0]$ loadings, respectively. With further increase in strain rate to 10^{11} s^{-1}, plastic deformation by only PT occurs for each direction (i.e. FCC-BCC for [100] loading and FCC-Amorphous for $[1\bar{1}0]$ and [111] loadings). Note that only crystalline PTs occur for the [100] loading, while loadings along $[1\bar{1}0]$ and [111] directions share the same PT path at a given strain rate except 10^9 s^{-1}. To sum up, we observe an overall transition of deformation mode from crystalline PTs to amorphization with increasing strain rate.

4. Discussion

In this work, we investigate PT mechanisms in CoCrNi MEAs with different local chemical environments. The PT is triggered by deformation under certain loading conditions in order to adapt to the external energy input. In the following discussion, we first consider the stability between FCC, BCC, HCP phases and amorphous state for rationalizing the change of PT paths. Then, we focus on the pressure thresholds of HCP and BCC phase nucleation as well as amorphization at various strain rates, in order to better understand the anisotropy and strain rate dependence of PTs.

4.1. The energetic stability of crystalline phases and amorphous state

To clarify the accuracy of the potential for MD simulations in capturing PT mechanisms, the difference of potential energy between FCC and HCP phases in random MEA at various temperatures under zero pressure is calculated (see supplementary material for details). As shown in Fig. 17(a), the potential energy difference between HCP phase and FCC phase remains negative up to 1200 K, which indicates that the HCP phase is favored over the FCC phase, especially in the cryogenic regime. As temperature rises, decreased stability of HCP phase is observed. The above results are consistent with density functional theory (DFT) calculations of the relative stability between HCP and FCC phases (Niu et al., 2018), and agree with the widely reported experimental observation of FCC-HCP PT in CoCrNi MEA at both cryogenic and room temperatures (Miao et al., 2017; Slone et al., 2018; He et al., 2021a), which suggests sufficient accuracy for this potential in describing PT path.

In contrast to the favored HCP phase, BCC and amorphous phases are unfavored against the FCC phase at ground state, since the potential energy of these two phases are higher than the FCC phase (Fig. 17(b)). However, the relative stability between HCP and BCC phases can be reversed under high pressure. As presented in Fig. 17(c) and (d), both HCP and BCC phases are energetically favored over the FCC phase under high pressure because the potential energy difference ($\Delta PE = PE_{HCP}\text{-}PE_{FCC}/PE_{BCC}\text{-}PE_{FCC}$) remains negative with rising temperature. In addition, HCP phase is the most favored structure under the pressure of 200 GPa but BCC phase becomes the most stable structure when pressure increases to 300 GPa, which explains the FCC-HCP-BCC PT in QI compression tests along the three loading orientations from the strain rate of 10^8 s^{-1} to 10^{10} s^{-1} (Table 3). Moreover, the energetic stability of the HCP and BCC phases declines (ΔPE increases) as the temperature increases. In contrast, the amorphous state with positive potential energy difference ($\Delta PE = PE_{Amorphous}\text{-}PE_{FCC}$) remains as the unfavored phase under high pressure though its stability improves with rising temperatures, implying a large activation energy barrier for triggering amorphization. Therefore, the effects of loading orientation, strain rate and CSRO should also be considered in respect of the initiation pressure of different PT paths, as we discussed below.

4.2. The pressure thresholds of different PT paths

Firstly, it should be noted that the PT proceeds by the nucleation and growth of embryos (Porter and Easterling, 2009; Nanev, 2020). In [100] loading with strain rates from 10^8 s^{-1} to 10^9 s^{-1}, the nucleation of incipient BCC clusters is the precursor for yielding, while subsequent formation of the HCP phase activates intense plastic deformation and suppresses the growth of the BCC clusters, as shown in Fig. 4(b). Thus, the formation of incipient BCC clusters at 10^8 s^{-1} and 10^9 s^{-1} is not considered a PT. However, at the strain rate of 10^{10} s^{-1}, incipient BCC clusters not only lead to the HCP phase formation, but also coalesce supporting the continuous growth of the BCC phase (Fig. 8). Hence this process is regarded as a FCC-BCC PT.

Secondly, to understand the occurrence of the PT, the initial moment of PT is considered as the critical strain when the corresponding phase content is over 3% (He et al., 2021a) according to Figs. 8, 12 and 16. However, it is worth noting that non-crystalline atoms can either appear along with dislocation activities and new crystalline phase boundaries, or prevail before HCP

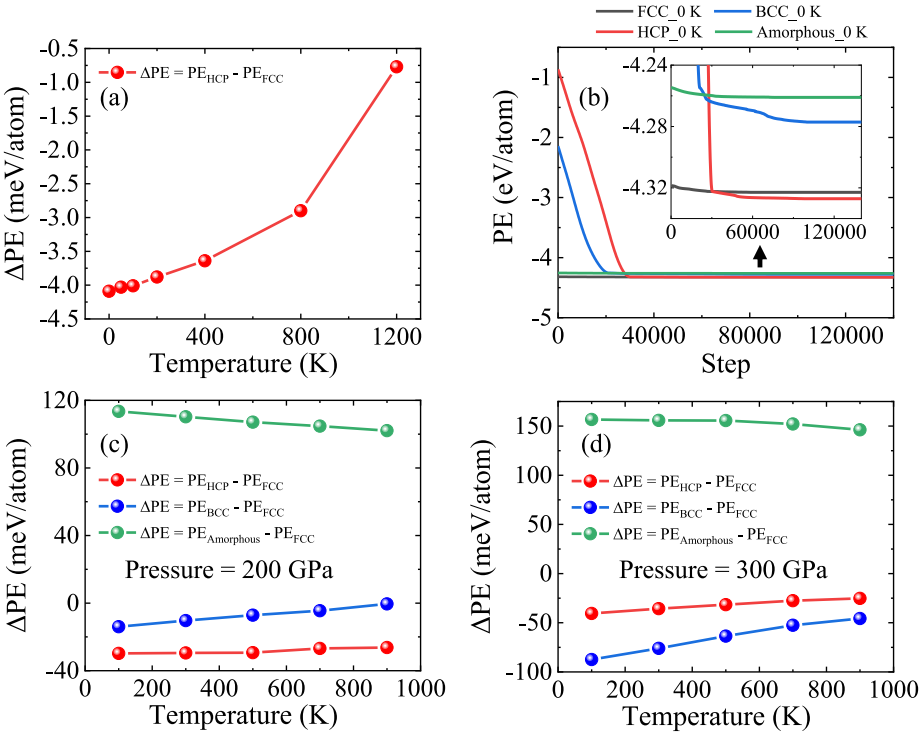

Fig. 17. (a) Potential energy (PE) difference between HCP and FCC phases as a function of temperature for random CoCrNi. (b) The potential energy variations of random CoCrNi sample with different phases during energy minimization. The relative potential energies of HCP, BCC, amorphous and FCC phases under the pressure of (c) 200 GPa and (d) 300 GPa as a function of temperature for random CoCrNi.

and BCC phase nucleation. Therefore, the criterion for the critical moment of amorphization should be carefully obtained based on a deformation mechanism. For $[1\bar{1}0]$ loading at the strain rates of 10^{10} s^{-1} and [111] loading at the strain rate of 10^{9} s^{-1}, amorphization is triggered by the accumulation of defects, thus the occurrence of amorphization is taken as the critical strain when non-crystalline atoms have larger content than HCP and BCC atoms (Figs. 12 and 16). For $[1\bar{1}0]$ loading at the strain rate of 10^{11} s^{-1} and [111] loading at 10^{10}~10^{11} s^{-1}, non-crystalline atoms predominate prior to the appearance of HCP and BCC structures; hence the criterion of non-crystalline phase content over 3% is adopted for the critical moment of amorphization (Figs. 12 and 16). The critical strains of different PT paths under three loading orientations at various strain rates are summarized in Table S1, S2 and S3, respectively. Accordingly, the pressure thresholds are shown in Fig. 18.

For FCC-HCP PT, prior normal impact experiment for FCC CrMnFeCoNi HEA showed that the PT threshold stress is significantly higher than 11 GPa at the strain rate of 5×10^{6} s^{-1} (Jiang et al., 2016). In addition, according to two independent *in situ* high-pressure experiments at ambient temperature, it was reported that the FCC to HCP PT in CrMnFeCoNi HEA starts at ~22 GPa and almost completes at ~41 GPa (Zhang et al., 2017); or starting at ~14 GPa and occurring up to a pressure of ~54.1 GPa (Tracy et al., 2017). In our MD simulations, the critical pressure for the FCC-HCP PT at the strain rates from 10^{8} s^{-1} to 10^{9} s^{-1} for the [100] loading falls within the range of 24–32 GPa, and that for $[1\bar{1}0]$ loading and [111] loading lies within 40 to 53 GPa and from 67 to 78 GPa, respectively. Regardless of the difference in chemical composition, compared to the above experiments, the critical pressures of FCC-HCP PT in simulation are, as expected, higher due to the high strain rate, yet they still have the same order, which can be considered reasonable to some extent.

One intuitive trend is that random MEA has the lowest critical pressure, while the critical pressure of FCC-HCP PT in 350KMDMC is close to or slightly lower than that in 950KMDMC. Such a trend is attributed to the combination effects of CSRO on bulk property and local energy barrier fluctuation of plasticity. On one hand, the average unstable stacking fault energy, intrinsic stacking fault energy and elastic modulus increase with increasing degree of CSRO (Ding et al., 2018; Li et al., 2019; Jian et al., 2020), which indicates that CSRO is supposed to raise the energy barrier of plasticity of the whole sample on average. On the other hand, local ordering cluster can provide easy nucleation sites for SFs since CoCr cluster has lower unstable stacking fault energy than random CoCrNi mixture and pure Ni (Jian et al., 2020), which means that it is harder for SFs to propagate away from the CoCr nucleation sites surrounded by Ni with higher degrees of CRSO.

To reach the critical HCP phase volume fraction of 3%, SFs not only need to nucleate from favorable sites, but also need to further propagate and grow into a larger phase, which implies that the FCC-HCP PT is affected by both the local energy fluctuation of stacking fault nucleation and the bulk plastic energy barrier. As a result, random MEA (without CSRO) possesses the lowest critical strain since the co-occurrence of stacking fault nucleation and propagation is relatively faster than sample with CSRO (Table

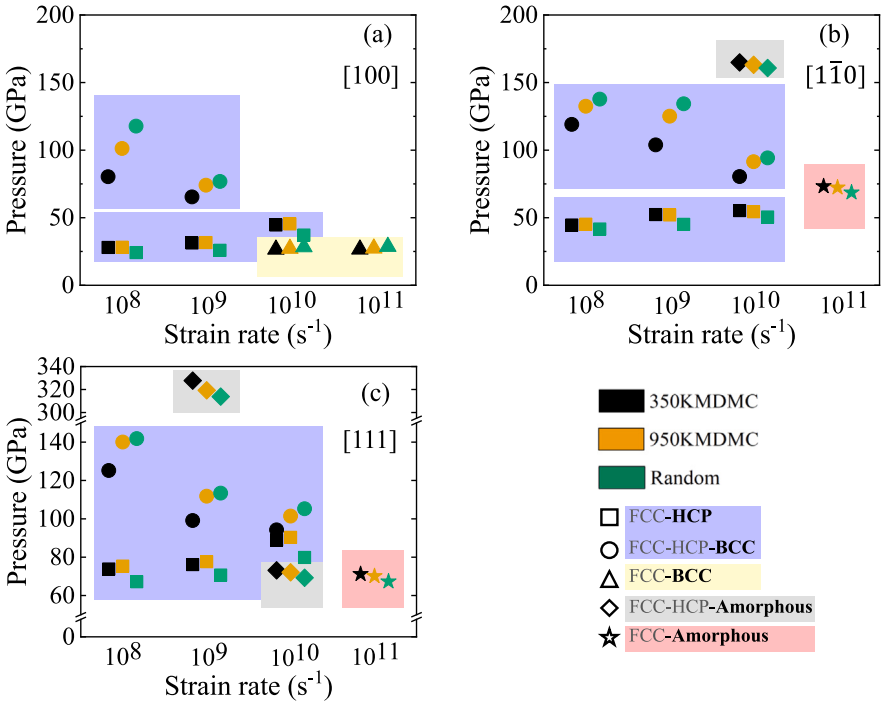

Fig. 18. The pressure for the initiation of different PT paths in three types of MEA under three loading orientations at various strain rates. The definitions of 350KMDMC, 950KMDMC, and random are consistent with those in Fig. 2.

S1–S3). Thus, the lowest critical strain and elastic modulus in random MEA leads to the smallest critical pressure. However, the combination effects of CSRO on bulk energy barrier and local energy fluctuation of plasticity may lead to a lower critical strain of FCC-HCP PT in 350KMDMC sample than that of 950KMDMC sample (Table S1–S3). Hence, a lower critical strain but higher elastic modulus of 350KMDMC sample could cause a similar or even slightly lower critical pressure of FCC-HCP PT than 950KMDMC sample. Nevertheless, the critical pressure of FCC-HCP PT in random MEA (without CSRO) is always lower than 350KMDMC and 950KMDMC samples (with CSRO) under three loading orientations. which indicates that the introduction of CSRO is able to raise the energy barrier of FCC-HCP PT.

For the initiation of BCC phase in three types of MEA, when compressed in different directions at the strain rate below 10^{10} s^{-1}, the BCC phase forms more easily (lower pressure threshold) in MEAs with higher degrees of CSRO, which can be explained by the more sluggish dislocation glide and more frequent HCP lath or SF interactions. Moreover, compared to [1$\bar{1}$0] and [111] loadings, compression in the [100] direction possesses lower critical pressure of BCC phase nucleation and thus leads to higher BCC phase content than in the other two directions (Figs. 8, 12 and 16) since the [100] direction favors the PT path towards BCC structure according to the Bain model (Bowles and Wayman, 1972), which also agrees with previous MPEA MD simulations (Chen et al., 2021a; Li et al., 2018a).Once the strain rate reaches or exceeds 10^{10} s^{-1}, the pressure threshold for BCC phase nucleation becomes lower than that for HCP phase nucleation for [100] loading, which indicates that FCC-HCP PT gives way to FCC-BCC PT. In contrast, for [1$\bar{1}$0] and [111] loading, BCC phase nucleation still relies on HCP interactions at the strain rate of 10^{10} s^{-1} and thus possessing a higher critical pressure than [100] loading.

For [1$\bar{1}$0] and [111] loading, numerous amorphous regions emerge along with the nucleation and propagation of many dislocations as an alternative deformation mechanism at the strain rate of 10^{10} s^{-1} (Figs. 11, 15, 12(c), and 16(c)). At the strain rate of 10^{11} s^{-1}, amorphization dominates deformation. The amorphization process is considered a general deformation mechanism for materials subjected to high stress states in confinement and/or during high strain rate deformation (Zhao et al., 2021a).

4.3. *The comparison between solid-state amorphization and virtual melting*

To further confirm whether the non-crystalline regions induced by extreme strain rate is solid-state amorphization, we estimate the diffusion coefficient D in three types of MEAs compressed along [111] direction at the strain rate of 10^{10} s^{-1}, [1$\bar{1}$0] and [111] directions at the strain rate of 10^{11} s^{-1} from the calculated mean squared displacement (MSD) during an extended equilibrium period of 100 ps (see supplementary material for details). The D values of representative atomic configurations with the initial development of non-crystalline atoms are all two to three orders of magnitude smaller than 10^{-9} m^2/s (Table S4), the typical value for liquid (Zhao et al., 2015; He et al., 2012), which indicates that the amorphization within MEAs is solid-state during QI compression rather than induced by the virtual melting (Levitas and Ravelo, 2012).

According to the results of Levitas and Ravelo (2012), virtual melting is activated locally (near the shock front) in pure metals by the work of high deviatoric stress which stimulates melting to proceed faster than the nucleation of dislocations, and the whole process only lasts in picosecond time scales. Then, the liquid region rapidly recrystallizes to a hydrostatically loaded crystal. In other words, virtual melting is an intermediate stage before defect (dislocations or twins) multiplications. However, in the present study, amorphization is either triggered by the accumulation of defect interactions or the large external energy input at extreme strain rates, leading to a homogeneous nucleation of disordered embryos which continue to grow and expand into larger phases with further loading. Such deformation/strain rate-induced solid-state amorphization is a continuous process, different from the prior non-hydrostatic stress-induced virtual melting mechanism.

While we only investigate the plastic deformation and PT mechanisms of single crystalline MPEAs using atomistic simulation at relatively high strain rate, the above results can provide insight into actual propensities of PTs in polycrystalline MPEAs by further considering the effects of GBs. As reported in a recent experimental study, the BCC phase nucleation at GBs along with dislocations and SFs prevails in the initial plastic deformation, while BCC phase formation at the intersections of HCP laths in the grain interior appears after shear band interactions (Bae et al., 2018). Nevertheless, grain coarsening decreases FCC stability and increases formation of the HCP phase, which leads to BCC phase nucleation inside the grains (Jo et al., 2021). Therefore, with increasing grain size and reduced GB content, the competition between the nucleation of the BCC phase at different sites (e.g., at GBs or intragranular HCP intersections), and the roles of strain rate and local orientation distribution in PTs, may be an important issue when investigating TRIP effects in polycrystalline MPEAs.

5. Conclusions

Using both hybrid Monte Carlo/molecular dynamics (MD) and large-scale MD simulations, we perform quasi-isentropic (QI) compression in single crystalline CoCrNi medium entropy alloy (MEA) along different crystallographic orientations ([100], $[1\bar{1}0]$, and [111]) to probe the dynamic responses and the corresponding mechanisms of plastic deformation and phase transition (PT) at various strain rates (10^8 s^{-1} to 10^{11} s^{-1}). The main findings are as follows.

- [100] direction favors the formation of the body-centered-cubic (BCC) phase. The nucleation of anomalous incipient BCC clusters at the initial deformation stage tends to occur at ordered CoCr regions and serve as the precursor of dislocation nucleation regardless of the strain rate, which causes insensitivity in the yield stress to strain rate. The face-centered cubic (FCC) to hexagonal-close-packed (HCP) PT is overwhelmed by the FCC-BCC PT as strain rate increases.
- The yield stress of $[1\bar{1}0]$ and [111] directions shows positive strain-rate sensitiveness. For the $[1\bar{1}0]$ loading, dislocation glide and FCC-HCP-BCC PT dominate the plastic deformation when the strain rate is below 10^{10} s^{-1}. For the [111] loading, the formation of amorphous regions aids in the plasticity after severe dislocation entanglement at large deformation. Further increases in strain rate leads to the domination of amorphization in plasticity and crystalline PTs are absent.
- While the HCP phase is the most energetically favored structure and BCC phase is unfavored against FCC phase for CoCrNi MEA at ground state, the relative stability of HCP and BCC phases can be reversed under high pressure.
- Although the chemical short-range order (CSRO) is not the origin of BCC phase nucleation, it indirectly facilitates the PT process by offering sluggish dislocation slip and promoting interactions among HCP laths and SFs.
- On the basis of crystallographic orientation, HCP and BCC phases as well as amorphization can be activated through different PT paths at certain strain rate in CoCrNi MPEA, displaying a promising polymorphism of this material. Once the large stress state is coupled with high strain rate, amorphization becomes a generalized deformation mechanism in such extreme regime.

CRediT authorship contribution statement

Zhuocheng Xie: Investigation, Formal analysis, Writing – original draft, Writing – review & editing. **Wu-Rong Jian:** Conceptualization, Investigation, Formal analysis, Supervision, Writing – review & editing. **Shuozhi Xu:** Formal analysis, Writing – review & editing. **Irene J. Beyerlein:** Formal analysis, Writing – review & editing. **Xiaoqing Zhang:** Formal analysis, Writing – review & editing. **Xiaohu Yao:** Formal analysis, Supervision, Writing – review & editing. **Run Zhang:** Formal analysis, Writing – review & editing.

Declaration of competing interest

The authors declare that they have no known competing financial interests or personal relationships that could have appeared to influence the work reported in this paper.

Acknowledgments

X.Y. would like to express his sincere gratitude for the financial support by National Science Foundation for Distinguished Young Scholars of China (11925203) and Natural Science Foundation of China (11672110). X.Z. acknowledges support from Natural Science Foundation of China (11972163). R.Z. gratefully acknowledges support from Natural Science Foundation of China (12172136).

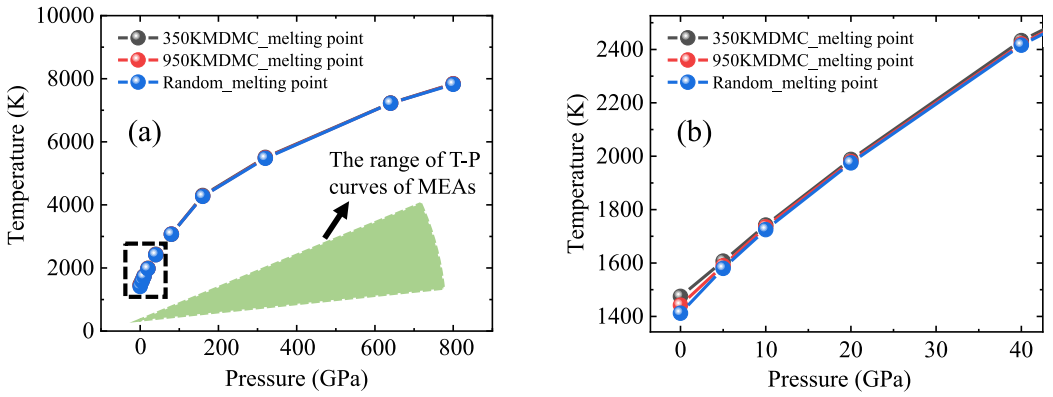

Fig. A.1. (a) The melting points of 350KMDMC, 950KMDMC, and random CoCrNi samples as the function of pressure determined by the solid–liquid coexistence method and the range of temperature–pressure (T–P) curves of all CoCrNi MEAs during QI compression at various strain rates (denoted by the green area). The melting lines of three MEAs are extremely close to each other in (a). Marked by the dashed rectangle, the linear stages of the melting lines are enlarged in (b). The definitions of the models are consistent with those in Fig. 2. (For interpretation of the references to color in this figure legend, the reader is referred to the web version of this article.)

Appendix A. Calculation of the melting points of MEAs

Using solid–liquid coexistence (two-phase) simulations (Morris et al., 1994; Chavoshi et al., 2017), we calculate the melting point of three CoCrNi MEAs as the function of pressure in Fig. A.1(a). The range of temperature–pressure (T–P) curves of all MEAs during QI compression at various strain rates is also shown in Fig. A.1(a) (denoted by the green area). All T–P curves lie respectively below the melting lines of the corresponding MEAs, indicating that melting does not occur and MEAs maintain solid state during compression. Marked by the dashed rectangle and Region B, the initial linear stage of each MEA melting line is enlarged in Fig. A.1(b). The higher degree of CSRO enhances the melting point of MEA slightly, similar to the result in the previous study (Jian et al., 2021), though the difference is moderate overall.

Appendix B. Supplementary data

Supplementary material related to this article can be found online at https://doi.org/10.1016/j.ijplas.2022.103389.

References

Antillon, E., Woodward, C., Rao, S., Akdim, B., Parthasarathy, T., 2020. Chemical short range order strengthening in a model FCC high entropy alloy. Acta Mater. 190, 29–42.
Bae, J.W., Seol, J.B., Moon, J., Sohn, S.S., Jang, M.J., Um, H.Y., Lee, B.-J., Kim, H.S., 2018. Exceptional phase-transformation strengthening of ferrous medium-entropy alloys at cryogenic temperatures. Acta Mater. 161, 388–399.
Bahramyan, M., Mousavian, R.T., Brabazon, D., 2020. Study of the plastic deformation mechanism of TRIP-TWIP high entropy alloys at the atomic level. Int. J. Plast. 127, 102649.
Bain, E.C., Dunkirk, N., 1924. The nature of martensite. Trans. Am. Inst. Min. Metall. Eng. 70 (1), 25–47.
Bowles, J., Wayman, C., 1972. The bain strain, lattice correspondences, and deformations related to martensitic transformations. Metall. Trans. 3 (5), 1113–1121.
Bridgman, P., 1956. High pressure polymorphism of iron. J. Appl. Phys. 27 (6), 659.
Bryukhanov, I., Kovalev, V., Larin, A., 2015. Nucleation of dislocations in aluminum alloys with copper. Phys. Solid State 57 (9), 1807–1817.
Cai, Y., Wang, L., Wu, H., Zhu, M., Liu, C., Luo, S., 2015. Homogeneous crystal nucleation in liquid copper under quasi-isentropic compression. Phys. Rev. B 92 (1), 014108.
Cao, F., Chen, Y., Zhao, S., Ma, E., Dai, L., 2021. Grain boundary phase transformation in a CrCoNi complex concentrated alloy. Acta Mater. 209, 116786.
Cao, F.-H., Wang, Y.-J., Dai, L.-H., 2020. Novel atomic-scale mechanism of incipient plasticity in a chemically complex CrCoNi medium-entropy alloy associated with inhomogeneity in local chemical environment. Acta Mater. 194, 283–294.
Chandan, A.K., Kishore, K., Hung, P.T., Ghosh, M., Chowdhury, S.G., Kawasaki, M., Gubicza, J., 2022. Effect of nickel addition on enhancing nano-structuring and suppressing TRIP effect in $Fe_{40}Mn_{40}Co_{10}Cr_{10}$ high entropy alloy during high-pressure torsion. Int. J. Plast. 150, 103193.
Chavoshi, S.Z., Xu, S., Goel, S., 2017. Addressing the discrepancy of finding the equilibrium melting point of silicon using molecular dynamics simulations. Proc. R. Soc. Lond. Ser. A Math. Phys. Eng. Sci. 473 (2202), 20170084.
Chen, S., Aitken, Z.H., Pattamatta, S., Wu, Z., Yu, Z.G., Srolovitz, D.J., Liaw, P.K., Zhang, Y.-W., 2021a. Simultaneously enhancing the ultimate strength and ductility of high-entropy alloys via short-range ordering. Nature Commun. 12 (1), 4953.
Chen, S., Oh, H.S., Gludovatz, B., Kim, S.J., Park, E.S., Zhang, Z., Ritchie, R.O., Yu, Q., 2020. Real-time observations of TRIP-induced ultrahigh strain hardening in a dual-phase CrMnFeCoNi high-entropy alloy. Nature Commun. 11 (1), 826.
Chen, X., Wang, Q., Cheng, Z., Zhu, M., Zhou, H., Jiang, P., Zhou, L., Xue, Q., Yuan, F., Zhu, J., Xiaolei, W., Ma, E., 2021b. Direct observation of chemical short-range order in a medium-entropy alloy. Nature 592, 712–716.
Chen, J., Yao, Z., Wang, X., Lu, Y., Wang, X., Liu, Y., Fan, X., 2018. Effect of c content on microstructure and tensile properties of as-cast CoCrFeMnNi high entropy alloy. Mater. Chem. Phys. 210, 136–145.
Cowley, J., 1950. An approximate theory of order in alloys. Phys. Rev. 77 (5), 669.

Dai, S.-C., Xie, Z.-C., Wang, Y.-J., 2021. Atomistic interpretation of extra temperature and strain-rate sensitivity of heterogeneous dislocation nucleation in a multi-principal-element alloy. Int. J. Plast. 103155.
Ding, J., Yu, Q., Asta, M., Ritchie, R.O., 2018. Tunable stacking fault energies by tailoring local chemical order in CrCoNi medium-entropy alloys. Proc. Natl. Acad. Sci. 115 (36), 8919–8924.
El-Atwani, O., Li, N., Li, M., Devaraj, A., Baldwin, J., Schneider, M.M., Sobieraj, D., Wróbel, J.S., Nguyen-Manh, D., Maloy, S.A., et al., 2019. Outstanding radiation resistance of tungsten-based high-entropy alloys. Sci. Adv. 5 (3), eaav2002.
Fang, Q., Chen, Y., Li, J., Jiang, C., Liu, B., Liu, Y., Liaw, P.K., 2019. Probing the phase transformation and dislocation evolution in dual-phase high-entropy alloys. Int. J. Plast. 114, 161–173.
de Fontaine, D., 1971. The number of independent pair-correlation functions in multicomponent systems. J. Appl. Crystall. 4 (1), 15–19.
Gludovatz, B., Hohenwarter, A., Catoor, D., Chang, E.H., George, E.P., Ritchie, R.O., 2014. A fracture-resistant high-entropy alloy for cryogenic applications. Science 345 (6201), 1153–1158.
Gludovatz, B., Hohenwarter, A., Thurston, K.V., Bei, H., Wu, Z., George, E.P., Ritchie, R.O., 2016. Exceptional damage-tolerance of a medium-entropy alloy CrCoNi at cryogenic temperatures. Nature Commun. 7 (1), 10602.
Hahn, E.N., Germann, T.C., Ravelo, R., Hammerberg, J.E., Meyers, M.A., 2017. On the ultimate tensile strength of tantalum. Acta Mater. 126, 313–328.
Hasan, M., Liu, Y., An, X., Gu, J., Song, M., Cao, Y., Li, Y., Zhu, Y., Liao, X., 2019. Simultaneously enhancing strength and ductility of a high-entropy alloy via gradient hierarchical microstructures. Int. J. Plast. 123, 178–195.
He, A., Duan, S., Shao, J.-L., Wang, P., Qin, C., 2012. Shock melting of single crystal copper with a nanovoid: Molecular dynamics simulations. J. Appl. Phys. 112 (7), 074116.
He, H., Naeem, M., Zhang, F., Zhao, Y., Harjo, S., Kawasaki, T., Wang, B., Wu, X., Lan, S., Wu, Z., et al., 2021a. Stacking fault driven phase transformation in CrCoNi medium entropy alloy. Nano Lett. 21 (3), 1419–1426.
He, F., Yang, Z., Liu, S., Chen, D., Lin, W., Yang, T., Wei, D., Wang, Z., Wang, J., Kai, J.-j., 2021b. Strain partitioning enables excellent tensile ductility in precipitated heterogeneous high-entropy alloys with gigapascal yield strength. Int. J. Plast. 144, 103022.
Higginbotham, A., Hawreliak, J., Bringa, E., Kimminau, G., Park, N., Reed, E., Remington, B., Wark, J., 2012. Molecular dynamics simulations of ramp-compressed copper. Phys. Rev. B 85 (2), 024112.
Hsieh, K.-T., Lin, Y.-Y., Lu, C.-H., Yang, J.-R., Liaw, P.K., Kuo, C.-L., 2020. Atomistic simulations of the face-centered-cubic-to-hexagonal-close-packed phase transformation in the equiatomic CoCrFeMnNi high entropy alloy under high compression. Comput. Mater. Sci. 184, 109864.
Hua, D., Xia, Q., Wang, W., Zhou, Q., Li, S., Qian, D., Shi, J., Wang, H., 2021. Atomistic insights into the deformation mechanism of a cocrNi medium entropy alloy under nanoindentation. Int. J. Plast. 142, 102997.
Jarmakani, H., McNaney, J., Kad, B., Orlikowski, D., Nguyen, J., Meyers, M., 2007. Dynamic response of single crystalline copper subjected to quasi-isentropic, gas-gun driven loading. Mater. Sci. Eng. A 463 (1–2), 249–262.
Jian, W.-R., Wang, L., Bi, W., Xu, S., Beyerlein, I.J., 2021. Role of local chemical fluctuations in the melting of medium entropy alloy CoCrNi. Appl. Phys. Lett. 119 (12), 121904.
Jian, W.-R., Xie, Z., Xu, S., Su, Y., Yao, X., Beyerlein, I.J., 2020. Effects of lattice distortion and chemical short-range order on the mechanisms of deformation in medium entropy alloy CoCrNi. Acta Mater. 199, 352–369.
Jian, W.-R., Xie, Z., Xu, S., Yao, X., Beyerlein, I.J., 2022. Shock-induced amorphization in medium entropy alloy CoCrNi. Scr. Mater. 209, 114379.
Jiang, Z., He, J., Wang, H., Zhang, H., Lu, Z., Dai, L., 2016. Shock compression response of high entropy alloys. Mater. Res. Lett. 4 (4), 226–232.
Jo, Y., Choi, W., Kim, D., Zargaran, A., Sohn, S.S., Kim, H.S., Lee, B., Kim, N.J., Lee, S., 2019. FCC to BCC transformation-induced plasticity based on thermodynamic phase stability in novel $V_{10}Cr_{10}Fe_{45}Co_xNi_{35-x}$ medium-entropy alloys. Sci. Rep. 9 (1), 2948.
Jo, Y.H., Kim, D.W., Kim, H.S., Lee, S., 2021. Effects of grain size on body-centered-cubic martensitic transformation in metastable $Fe_{46}Co_{30}Cr_{10}Mn_5Si_7V_2$ high-entropy alloy. Scri. Mater. 194, 113620.
Kim, J.-K., Kim, J.H., Park, H., Kim, J.-S., Yang, G., Kim, R., Song, T., Suh, D.-W., Kim, J., 2022. Temperature-dependent universal dislocation structures and transition of plasticity enhancing mechanisms of the Fe40Mn40Co10Cr10 high entropy alloy. Int. J. Plast. 148, 103148.
Korchuganov, A.V., Tyumentsev, A.N., Zolnikov, K.P., Litovchenko, I.Y., Kryzhevich, D.S., Gutmanas, E., Li, S., Wang, Z., Psakhie, S.G., 2019a. Nucleation of dislocations and twins in fcc nanocrystals: Dynamics of structural transformations. J. Mater. Sci. Technol. 35 (1), 201–206.
Korchuganov, A.V., Zolnikov, K.P., Kryzhevich, D.S., 2019b. Atomic mechanisms of stacking fault propagation in copper crystallite. Mater. Lett. 252, 194–197.
Kumar, N.K., Li, C., Leonard, K., Bei, H., Zinkle, S., 2016. Microstructural stability and mechanical behavior of FeNiMnCr high entropy alloy under ion irradiation. Acta Mater. 113, 230–244.
Kurdjumov, G., Sachs, G., 1930. Over the mechanisms of steel hardening. Z. Phys. 64, 325–343.
Lane, J.M.D., Foiles, S.M., Lim, H., Brown, J.L., 2016. Strain-rate dependence of ramp-wave evolution and strength in tantalum. Phys. Rev. B 94 (6), 064301.
Laplanche, G., Schneider, M., Scholz, F., Frenzel, J., Eggeler, G., Schreuer, J., 2020. Processing of a single-crystalline CrCoNi medium-entropy alloy and evolution of its thermal expansion and elastic stiffness coefficients with temperature. Scr. Mater. 177, 44–48.
Levitas, V.I., Ravelo, R., 2012. Virtual melting as a new mechanism of stress relaxation under high strain rate loading. Proc. Natl. Acad. Sci. 109 (33), 13204–13207.
Li, J., Chen, H., Fang, Q., Jiang, C., Liu, Y., Liaw, P.K., 2020. Unraveling the dislocation–precipitate interactions in high-entropy alloys. Int. J. Plast. 133, 102819.
Li, L., Chen, Z., Kuroiwa, S., Ito, M., Kishida, K., Inui, H., George, E.P., 2022. Tensile and compressive plastic deformation behavior of medium-entropy Cr-Co-Ni single crystals from cryogenic to elevated temperatures. Int. J. Plast. 148, 103144.
Li, J., Fang, Q., Liu, B., Liu, Y., 2018a. Transformation induced softening and plasticity in high entropy alloys. Acta Mater. 147, 35–41.
Li, W., Hahn, E.N., Branicio, P.S., Yao, X., Zhang, X., Feng, B., Germann, T.C., 2021a. Rate dependence and anisotropy of SiC response to ramp and wave-free quasi-isentropic compression. Int. J. Plast. 138, 102923.
Li, Z., Körmann, F., Grabowski, B., Neugebauer, J., Raabe, D., 2017a. Ab initio assisted design of quinary dual-phase high-entropy alloys with transformation-induced plasticity. Acta Mater. 136, 262–270.
Li, Z., Pradeep, K.G., Deng, Y., Raabe, D., Tasan, C.C., 2016. Metastable high-entropy dual-phase alloys overcome the strength–ductility trade-off. Nature 534 (7606), 227–230.
Li, Q.-J., Sheng, H., Ma, E., 2019. Strengthening in multi-principal element alloys with local-chemical-order roughened dislocation pathways. Nature Commun. 10 (1), 3563.
Li, W., Xie, D., Li, D., Zhang, Y., Gao, Y., Liaw, P.K., 2021b. Mechanical behavior of high-entropy alloys. Prog. Mater. Sci. 118, 100777.
Li, Z., Zhao, S., Alotaibi, S.M., Liu, Y., Wang, B., Meyers, M.A., 2018b. Adiabatic shear localization in the CrMnFeCoNi high-entropy alloy. Acta Mater. 151, 424–431.
Li, Z., Zhao, S., Diao, H., Liaw, P., Meyers, M., 2017b. High-velocity deformation of $Al_{0.3}$CoCrFeNi high-entropy alloy: remarkable resistance to shear failure. Sci. Rep. 7, 42742.
Liu, X., Feng, H., Wang, J., Chen, X., Jiang, P., Yuan, F., Li, H., Ma, E., Wu, X., 2021. Mechanical property comparisons between CrCoNi medium-entropy alloy and 316 stainless steels. J. Mater. Sci. Technol. 108, 256–269.
Liu, S., Wu, Y., Wang, H., Lin, W., Shang, Y., Liu, J., An, K., Liu, X., Wang, H., Lu, Z., 2019. Transformation-reinforced high-entropy alloys with superior mechanical properties via tailoring stacking fault energy. J. Alloys Compd. 792, 444–455.
Lorenz, K., Edwards, M., Jankowski, A., Pollaine, S., Smith, R., Remington, B., 2006. High pressure, quasi-isentropic compression experiments on the Omega laser. High Energy Density Phys. 2 (3–4), 113–125.

Luo, B., Chen, X., Wang, G., Tan, F., Chen, G., Zhao, J., Sun, C., 2017. Dynamic strength measurement of aluminum under magnetically driven ramp wave pressure-shear loading. Int. J. Impact Eng. 100, 56–61.
Ma, Y., Yuan, F., Yang, M., Jiang, P., Ma, E., Wu, X., 2018. Dynamic shear deformation of a CrCoNi medium-entropy alloy with heterogeneous grain structures. Acta Mater. 148, 407–418.
Maity, T., Prashanth, K.G., Balcı, O., Kim, J.T., Schöberl, T., Wang, Z., Eckert, J., 2018. Influence of severe straining and strain rate on the evolution of dislocation structures during micro-/nanoindentation in high entropy lamellar eutectics. Int. J. Plast. 109, 121–136.
Miao, J., Slone, C., Smith, T., Niu, C., Bei, H., Ghazisaeidi, M., Pharr, G., Mills, M.J., 2017. The evolution of the deformation substructure in a Ni-Co-Cr equiatomic solid solution alloy. Acta Mater. 132, 35–48.
Ming, K., Bi, X., Wang, J., 2019. Strength and ductility of CrFeCoNiMo alloy with hierarchical microstructures. Int. J. Plast. 113, 255–268.
Ming, K., Lu, W., Li, Z., Bi, X., Wang, J., 2020. Amorphous bands induced by low temperature tension in a non-equiatomic CrMnFeCoNi alloy. Acta Mater. 188, 354–365.
Morris, J.R., Wang, C., Ho, K., Chan, C., 1994. Melting line of aluminum from simulations of coexisting phases. Phys. Rev. B 49 (5), 3109.
Moulton, B., Zaworotko, M.J., 2001. From molecules to crystal engineering: supramolecular isomerism and polymorphism in network solids. Chem. Rev. 101 (6), 1629–1658.
Nanev, C.N., 2020. Evaluation of the critical nucleus size without using interface free energy. J. Cryst. Growth 535, 125521.
Nene, S.S., Frank, M., Liu, K., Mishra, R., McWilliams, B., Cho, K., 2018a. Extremely high strength and work hardening ability in a metastable high entropy alloy. Sci. Rep. 8 (1), 9920.
Nene, S., Sinha, S., Frank, M., Liu, K., Mishra, R., McWilliams, B., Cho, K., 2018b. Unexpected strength–ductility response in an annealed, metastable, high-entropy alloy. Appl. Mater. Today 13, 198–206.
Niu, C., LaRosa, C.R., Miao, J., Mills, M.J., Ghazisaeidi, M., 2018. Magnetically-driven phase transformation strengthening in high entropy alloys. Nature Commun. 9 (1), 1–9.
Plimpton, S., 1995. Fast parallel algorithms for short-range molecular dynamics. J. Comput. Phys. 117 (1), 1–19.
Porter, D.A., Easterling, K.E., 2009. Phase Transformations in Metals and Alloys (Revised Reprint). CRC Press.
Qi, Y., Zhao, M., Feng, M., 2021. Molecular simulation of microstructure evolution and plastic deformation of nanocrystalline CoCrFeMnNi high-entropy alloy under tension and compression. J. Alloys Compd. 851, 156923.
Qiu, Y., Thomas, S., Fabijanic, D., Barlow, A., Fraser, H., Birbilis, N., 2019. Microstructural evolution, electrochemical and corrosion properties of AlxCoCrFeNiTiy high entropy alloys. Mater. Des. 170, 107698.
Ravelo, R., Holian, B.L., Germann, T.C., 2009. High strain rates effects in quasi-isentropic compression of solids. AIP Conf. Proc. 1195 (1), 825–828.
Romero, R.A., Xu, S., Jian, W.-R., Beyerlein, I.J., Ramana, C., 2022. Atomistic simulations of the local slip resistances in four refractory multi-principal element alloys. Int. J. Plast. 149, 103157.
Schneider, M., George, E., Manescau, T., Záležák, T., Hunfeld, J., Dlouhỳ, A., Eggeler, G., Laplanche, G., 2020. Analysis of strengthening due to grain boundaries and annealing twin boundaries in the CrCoNi medium-entropy alloy. Int. J. Plast. 124, 155–169.
Seagle, C., Davis, J.-P., Martin, M., Hanshaw, H., 2013. Shock-ramp compression: Ramp compression of shock-melted tin. Appl. Phys. Lett. 102 (24), 244104.
Sheng, H., Liu, H., Cheng, Y., Wen, J., Lee, P., Luo, W., Shastri, S., Ma, E., 2007. Polyamorphism in a metallic glass. Nature Mater. 6 (3), 192–197.
Shi, Y., Yang, B., Xie, X., Brechtl, J., Dahmen, K.A., Liaw, P.K., 2017. Corrosion of AlxCoCrFeNi high-entropy alloys: Al-content and potential scan-rate dependent pitting behavior. Corros. Sci. 119, 33–45.
Slone, C., Chakraborty, S., Miao, J., George, E.P., Mills, M.J., Niezgoda, S., 2018. Influence of deformation induced nanoscale twinning and FCC-HCP transformation on hardening and texture development in medium-entropy CrCoNi alloy. Acta Mater. 158, 38–52.
Smith, L.T., Su, Y., Xu, S., Hunter, A., Beyerlein, I.J., 2020. The effect of local chemical ordering on Frank-Read source activation in a refractory multi-principal element alloy. Int. J. Plast. 134, 102850.
Stukowski, A., 2009. Visualization and analysis of atomistic simulation data with OVITO–the Open Visualization Tool. Model. Simul. Mater. Sci. Eng. 18 (1), 015012.
Stukowski, A., Bulatov, V.V., Arsenlis, A., 2012. Automated identification and indexing of dislocations in crystal interfaces. Model. Simul. Mater. Sci. Eng. 20 (8), 085007.
Tracy, C.L., Park, S., Rittman, D.R., Zinkle, S.J., Bei, H., Lang, M., Ewing, R.C., Mao, W.L., 2017. High pressure synthesis of a hexagonal close-packed phase of the high-entropy alloy CrMnFeCoNi. Nature Commun. 8 (1), 15634.
Uzer, B., Picak, S., Liu, J., Jozaghi, T., Canadinc, D., Karaman, I., Chumlyakov, Y., Kireeva, I., 2018. On the mechanical response and microstructure evolution of NiCoCr single crystalline medium entropy alloys. Mater. Res. Lett. 6 (8), 442–449.
Vogler, T., Ao, T., Asay, J.R., 2009. High-pressure strength of aluminum under quasi-isentropic loading. Int. J. Plast. 25 (4), 671–694.
Wang, H., Chen, D., An, X., Zhang, Y., Sun, S., Tian, Y., Zhang, Z., Wang, A., Liu, J., Song, M., et al., 2021. Deformation-induced crystalline-to-amorphous phase transformation in a CrMnFeCoNi high-entropy alloy. Sci. Adv. 7 (14), eabe3105.
Wang, K., Chen, J., Zhu, W., Hu, W., Xiang, M., 2017. Phase transition of iron-based single crystals under ramp compressions with extreme strain rates. Int. J. Plast. 96, 56–80.
Wu, Y., Bönisch, M., Alkan, S., Abuzaid, W., Sehitoglu, H., 2018. Experimental determination of latent hardening coefficients in FeMnNiCoCr. Int. J. Plast. 105, 239–260.
Xiang, M., Chen, J., Su, R., 2016. Spalling behaviors of Pb induced by ramp-wave-loading: Effects of the loading rise time studied by molecular dynamics simulations. Comput. Mater. Sci. 117, 370–379.
Xiao, J., Deng, C., 2020. Martensite transformation induced superplasticity and strengthening in single crystalline CoNiCrFeMn high entropy alloy nanowires: A molecular dynamics study. Mater. Sci. Eng. A 793, 139853.
Xie, Z., Jian, W.-R., Xu, S., Beyerlein, I.J., Zhang, X., Wang, Z., Yao, X., 2021. Role of local chemical fluctuations in the shock dynamics of medium entropy alloy CoCrNi. Acta Mater. 221, 117380.
Yang, J., Jo, Y.H., Kim, D.W., Choi, W.-M., Kim, H.S., Lee, B.-J., Sohn, S.S., Lee, S., 2020a. Effects of transformation-induced plasticity (TRIP) on tensile property improvement of $Fe_{45}Co_{30}Cr_{10}V_{10}Ni_{5-x}Mn_x$ high-entropy alloys. Mater. Sci. Eng. A 772, 138809.
Yang, X.-S., Sun, S., Zhang, T.-Y., 2015. The mechanism of bcc α nucleation in single hcp ε laths in the fcc $\gamma \rightarrow$ hcp $\varepsilon \rightarrow$ bcc α martensitic phase transformation. Acta Mater. 95, 264–273.
Yang, Y., Yang, S., Wang, H., 2020b. Effects of microstructure on the evolution of dynamic damage of $Fe_{50}Mn_{30}Co_{10}Cr_{10}$ high entropy alloy. Mater. Sci. Eng. A 140440.
Yang, Y., Yang, S., Wang, H., 2020c. Effects of the phase content on dynamic damage evolution in $Fe_{50}Mn_{30}Co_{10}Cr_{10}$ high entropy alloy. J. Alloys Compd. 851, 156883.
Yin, S., Ding, J., Asta, M., Ritchie, R.O., 2020. Ab initio modeling of the energy landscape for screw dislocations in body-centered cubic high-entropy alloys. Npj Comput. Mater. 6 (1), 110.
Zeng, Q.-s., Ding, Y., Mao, W.L., Yang, W., Sinogeikin, S.V., Shu, J., Mao, H.-k., Jiang, J., 2010. Origin of pressure-induced polyamorphism in $Ce_{75}Al_{25}$ metallic glass. Phys. Rev. Lett. 104 (10), 105702.
Zhang, J., He, Q., Li, J., Yang, Y., 2021. Chemical fluctuation enabling strength-plasticity synergy in metastable single-phase high entropy alloy film with gigapascal yield strength. Int. J. Plast. 139, 102951.

Zhang, T., Ma, S., Zhao, D., Wu, Y., Zhang, Y., Wang, Z., Qiao, J., 2020a. Simultaneous enhancement of strength and ductility in a NiCoCrFe high-entropy alloy upon dynamic tension: Micromechanism and constitutive modeling. Int. J. Plast. 124, 226–246.
Zhang, N., Tang, Z., Lin, Z., Cai, Y., Chen, S., Lu, L., Zhao, X., Luo, S., 2022. Deformation and damage of heterogeneous structured high-entropy alloy CrMnFeCoNi under plate impact. Mater. Sci. Eng. A 143069.
Zhang, F., Wu, Y., Lou, H., Zeng, Z., Prakapenka, V.B., Greenberg, E., Ren, Y., Yan, J., Okasinski, J.S., Liu, X., et al., 2017. Polymorphism in a high-entropy alloy. Nature Commun. 8 (1), 15687.
Zhang, R., Zhao, S., Ding, J., Chong, Y., Jia, T., Ophus, C., Asta, M., Ritchie, R.O., Minor, A.M., 2020b. Short-range order and its impact on the CrCoNi medium-entropy alloy. Nature 581 (7808), 283–287.
Zhang, T., Zhao, R., Wu, F., Lin, S., Jiang, S., Huang, Y., Chen, S., Eckert, J., 2020c. Transformation-enhanced strength and ductility in a FeCoCrNiMn dual phase high-entropy alloy. Mater. Sci. Eng. A 780, 139182.
Zhao, F., Li, B., Jian, W., Wang, L., Luo, S., 2015. Shock-induced melting of honeycomb-shaped Cu nanofoams: Effects of porosity. J. Appl. Phys. 118 (3), 035904.
Zhao, S., Li, B., Remington, B., Wehrenberg, C., Park, H., Hahn, E., Meyers, M., 2021a. Directional amorphization of covalently-bonded solids: A generalized deformation mechanism in extreme loading. Mater. Today 49, 59–67.
Zhao, S., Li, Z., Zhu, C., Yang, W., Zhang, Z., Armstrong, D.E., Grant, P.S., Ritchie, R.O., Meyers, M.A., 2021b. Amorphization in extreme deformation of the CrMnFeCoNi high-entropy alloy. Sci. Adv. 7 (5), eabb3108.
Zhou, L., Wang, Q., Wang, J., Chen, X., Jiang, P., Zhou, H., Yuan, F., Wu, X., Cheng, Z., Ma, E., 2022. Atomic-scale evidence of chemical short-range order in CrCoNi medium-entropy alloy. Acta Mater. 224, 117490.